The Physics of Chromospheres and Coronae

P. Ulmschneider

Institut für Theoretische Astrophysik, Univ. Heidelberg,
Tiergartenstr. 15, 69121 Heidelberg, Germany
email: ulm@ita.uni-heidelberg.de

Abstract. Towards the goal to unravel the physical reasons for the existence of chromospheres and coronae significant progress has been made. Chromospheres and coronae are layers which are dominated by mechanical heating and usually by magnetic fields. The heating of chromospheres can be explained by an ordered sequence of different processes which systematically vary as function of height in the star and with the speed of its rotation. It seems now pretty certain that acoustic waves heat the low and middle chromosphere, and MHD waves the magnetic regions up to the high chromosphere. With faster rotation, the magnetic regions become more dominant. It seems that the highest chromosphere needs additional non-wave heating mechanisms and that there possibly reconnective microflare heating comes into play. For the corona many different heating processes occur which work in the various field geometries. Here more study is needed to identify the relevance of these various processes.

1 Introduction, What are Chromospheres and Coronae?

Already in antiquity the interested observer wondered about the *corona* (crown), the faint extended and spiky white shell around the Sun which becomes visible during a total solar eclipse, when the Moon hides the luminous solar disk (photosphere). We know today that the corona is composed of three components, the F-corona (F stands for Fraunhofer lines) which arises from dust particles which scatter the bright photospheric light spectrum with its absorption lines into the eye of the observer, the K-corona (K stands for Kontinuum) which consists of photospheric light devoid of spectral lines scattered by free electrons, and the E-corona (where E stands for emission lines among which the green and red coronal lines are the most prominent). It was B. Edlén and W. Grotrian who succeeded around 1940 to identify these coronal lines as iron lines from very high ionisation stages. The strongest green corona line at wavelength 5303 Å originates from Fe XIV, while the red one at 6375 Å from Fe X. The presence of such lines demonstrated that the corona is a gas with temperatures of many millions K. This high temperature explains why the energy of the electrons is so large that without great effort, by collisional impact, they strip away 9 to 13 electrons from the iron atoms. It also explains why the scattering of the photospheric light by the fast moving electrons results in a continuous spectrum.

While the corona extends to many solar radii the *chromosphere* is a layer of only 2 to 3 thousand km thickness which becomes visible near the start and end of a total eclipse. The chromosphere got its name from the prominent red emission of the Hα line of neutral hydrogen at 6563 Å. The chromosphere is a

layer where the temperature rises from photospheric values of between 4000 and 6000 K to about 20 000 K and where neutral hydrogen is still present. In the region of a few 100 km thickness between the chromosphere and corona, called *transition layer*, hydrogen becomes ionised and the temperature increases from 20 000 to millions of K.

Observations show that essentially all late-type stars with surface convection zones have chromospheres and that most of them also possess coronae. The presence of chromospheres in stars other than the Sun is indicated e.g., by emission cores in the Ca II H and K as well as the Mg II h and k lines while coronae are detected by e.g., the presence of C IV and Mg X lines as well as the X-ray emission. The surprising fact is that the coronal temperatures (of 1 to 6 million K) are almost as high as the temperatures in the solar core, where the nuclear processes take place and where the energy for the solar luminous radiation is generated. Also surprising is the fact that the density in the short extent of the photosphere and chromosphere decreases by 8 orders of magnitude (from $\rho = 3 \times 10^{-7}$ to 3×10^{-15} g cm^{-3}) which is similar to the 9 orders of magnitude density decrease (from $\rho = 200$ to 2×10^{-7} g cm^{-3}) which occurs from the solar core to the solar surface but over a much larger distance of 700 000 km.

With an underlying photosphere, where the temperature decreases from values close to the effective temperature (of 5770 K for the Sun) to a minimum temperature of about 4000 K, the question is why are these chromospheric and coronal layers so hot and why are they so different from the photosphere? This question has to be answered by realising that a single main-sequence star like our Sun is uniquely characterised by specifying four independent parameters and that isolated stars such as our Sun, except in their initial T-Tauri phase, are not influenced by the surrounding interstellar medium. With the next stars several light years away, it is clear that not only the solar interior and the photosphere, but also the chromosphere and corona must be uniquely determined by these four parameters. We therefore face the great challenge to unravel the physical reasons how on basis of four parameters the average structure of the chromospheres and coronae are precisely and uniquely determined. This aim has so far not been fully realised but significant progress has been made towards this goal and towards the clarification of the physics of chromospheres and coronae.

That four parameters are sufficient to uniquely characterise a main-sequence star can be seen by considering the state when after its pre main-sequence evolution the star reaches the Zero Age Main Sequence (ZAMS) phase. Here it is homogeneous and can be described by its total mass $M_\star$ and metallicity (metal content or chemical composition) Z_m. Although stars can have peculiar element abundances, the majority of stars can be well characterised by a single metallicity ratio Z_m which gives the stellar abundances of the elements heavier than He (called metals) in terms of the solar metal abundances (see below). The elapsed time t_S since the ZAMS phase is then a crucial third parameter which characterises the present state of the star.

The low rotation rate of late-type main-sequence stars indicates that they have lost their primordial magnetic field and it is generally agreed that the

present magnetic field of these stars is newly generated from the *dynamo mechanism* which works efficiently only when rotation and convection are both present. The rotation period $P_{\rm Rot}$ thus is a fourth essential parameter which characterises a star. There is the difficulty that there is no unique rotation period for a star. As discussed in the contributions of Antia and Venkatakrishnan (this volume), our Sun due to the differential rotation has a sidereal surface rotation rate which varies from 15° to 11° per day between 0 and 60° latitude. This amounts to a latitudinal variation of the rotation period from 24 to 33 days. However, the Sun with an average rotation period of $P_{\rm Rot} = 28 \pm 4$ days can still be considered to belong to the group of slow rotators (see Fig. 45).

One might have the fortunate case, that for some single stars $P_{\rm Rot}$, due to a similar rotational braking history, is a known function of $t_{\rm S}$ which would reduce the basic parameters to only three. However, because more than 70% of the stars are members of multiple systems where unknown amounts of orbital angular momentum was converted into spin angular momentum, $P_{\rm Rot}$ usually should be taken as an independent parameter. For practical purposes these four independent parameters $M_\star$, $Z_{\rm m}$, $t_{\rm S}$, $P_{\rm Rot}$ can finally be expressed by four more convenient parameters $T_{\rm eff}$, g, $Z_{\rm m}$, $P_{\rm Rot}$, where $T_{\rm eff}$ is the effective temperature and g the surface gravity.

2 Heating Mechanisms

The conservation of energy in a gas element somewhere in the chromosphere can be written as

$$\frac{\partial}{\partial t}\left(\frac{1}{2}\rho v^2 + \rho c_V T + \rho\phi\right) + \boldsymbol{\nabla}\cdot\rho\mathbf{v}\left(\frac{1}{2}v^2 + c_V T + \frac{p}{\rho} + \phi\right) = \left.\frac{{\rm d}Q}{{\rm d}t}\right|_{\rm Mech} + 4\pi\kappa\,(J-B)\ . \tag{1}$$

Here $\frac{1}{2}\rho v^2$ is the kinetic, $\rho c_V T$ the internal and $\rho\phi$ the potential energy density (in erg cm^{-3}), where the gravitational potential is given by $\phi = -GM_\odot/r$ with G, $M_\odot$, r being the gravitational constant, the solar mass, and the radial distance of the gas element from the centre of the Sun, respectively. ρ is the density, p the gas pressure, c_V the specific heat at constant volume, T the temperature and v the flow speed of the solar wind. The three energy flux components in (erg cm^{-2} s^{-1}) are the kinetic energy flux $\rho\mathbf{v}\frac{1}{2}v^2$, the enthalpy flux $\rho\mathbf{v}\,(c_V T + p/\rho)$ and the potential energy flux $\rho\mathbf{v}\phi$. On the right hand side, we have the heat addition by mechanical heating in which we also include magnetic heating, and radiative heating. For simplicity, radiative heating is written in terms of a gray (i.e., frequency independent) Rosseland opacity κ (e.g., given by (10)) times the mean intensity J minus the source function for which we take the frequency integrated Planck function B.

As the chromosphere and the corona surround the solar surface since billions of years and as the mass flux ρv of the solar wind is undetectably small at

chromospheric and low coronal heights, one can neglect both terms of the left hand side of (1) and gets essentially a balance of mechanical heating and radiative cooling:

$$\left.\frac{\mathrm{d}Q}{\mathrm{d}t}\right|_{\mathrm{Mech}} = 4\pi\kappa\,(B - J)\ . \tag{2}$$

The mean intensity and the Planck function can be written

$$J = \frac{1}{2}\frac{\sigma}{\pi}T_{\mathrm{eff}}^4\ , \qquad B = \frac{\sigma}{\pi}T^4\ , \tag{3}$$

where σ is the Stefan–Boltzmann constant where the factor $1/2$ in J comes from the fact that above the solar surface there is only outgoing radiation.

If we neglect mechanical heating, then radiative heating alone must be zero. This is the condition of *radiative equilibrium* which is the physical basis of stellar photospheres (in deeper photospheric layers, however, convective energy transport must be considered in addition to the transport by radiation). In radiative equilibrium one has $J = B$, that is, the photospheric temperature should decrease in outward direction until a boundary temperature of $T = 2^{-1/4}T_{\mathrm{eff}} \approx 0.8T_{\mathrm{eff}}$ is reached. For the Sun with $T_{\mathrm{eff}} = 5770\,\mathrm{K}$ one would have a boundary temperature of $T \approx 4850\,\mathrm{K}$.

From the observed high temperatures of 20 000 to millions K in chromospheres and coronae one must have using (3) that $B \gg J$, which implies large and persistent amounts of mechanical heating to satisfy (2). In contrast to photospheres, *chromospheres and corona are thus characterised as layers which require large amounts of mechanical heating.*

Table 1 summarises the mechanisms which are thought to provide a steady supply of mechanical energy to balance the chromospheric and coronal energy losses. The term heating mechanism comprises three physical aspects, the *generation* of a carrier of mechanical energy, the *transport* of mechanical energy into the chromosphere and corona and the *dissipation* of the energy in these layers. Table 1 shows the various proposed energy carriers which can be classified into two main categories: *hydrodynamic* and *magnetic* mechanisms. The magnetic mechanisms can be subdivided further into wave- or *AC-mechanisms* and current sheet- or *DC-mechanisms*. Also in Table 1 the mode of dissipation of these mechanical energy carriers is indicated. For more details see Narain & Ulmschneider (1990, 1996), as well as Ulmschneider (1996)

Ultimately, these mechanical carriers derive their energy from the nuclear processes in the stellar core from where it is transported in the form of radiation and convection to the stellar surface. In late-type stars the mechanical energy generation is caused by the gas motions of the surface convection zones. These gas motions are largest in the regions of smallest density near the top boundary of the convection zone. Due to this the mechanical energy, particularly the wave energy, is generated in a narrow surface layer.

Let us now discuss the various mechanisms. All of them have been found to work in terrestrial applications and thus should also work in a stellar environment. However, the problem is to identify which of these mechanisms are

Table 1. Heating mechanisms

energy carrier	*dissipation mechanism*
hydrodynamic heating mechanisms	
acoustic waves, $P<P_A$	shock dissipation
pulsational waves, $P \geq P_A$	shock dissipation
magnetic heating mechanisms	
1. alternating current (AC) or wave mechanisms	
slow mode MHD waves, longitudinal MHD tube waves	shock dissipation
fast mode MHD waves	Landau damping
Alfvén waves (transverse, torsional)	mode-coupling resonance heating turbulent heating compressional viscous heating ion-cyclotron resonance heating Landau damping
magnetoacoustic surface waves	mode-coupling phase-mixing resonant absorption
2. direct current (DC) mechanisms	
current sheets	reconnection (turbulent heating, wave heating)

dominant and if so, in what regions and situations do these various mechanisms work. At the present time the heating processes in the corona and even in the high chromosphere are not yet fully clarified and for instance there is the debate whether AC or DC-mechanisms are more important in these layers. Also there is the question of what is the role of surface waves propagating along magnetic flux tubes. Only careful studies can clarify the hierarchy of the heating mechanisms in chromospheres and coronae.

3 Hydrodynamic Heating Mechanisms

There are two types of hydrodynamic mechanisms, *acoustic waves* and *pulsational waves*. The convection zone like every turbulent flow field generates *acoustic waves* which propagate in all directions. Even if the wave energy due to radiative damping is not fully conserved, acoustic waves which propagate in outward direction will suffer a large growth of the wave amplitude due to the strong density decrease. Because of nonlinear processes the wave profile gets distorted and shocks form which then dissipate the wave energy and heat the atmosphere (see Fig. 1). *Pulsational waves* which occur e.g., in Mira stars are

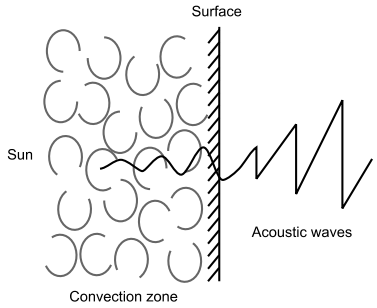

Fig. 1. Acoustic waves and the heating by shocks

another hydrodynamic heating mechanism which propagate to the outer stellar atmosphere where they also dissipate through shocks.

Acoustic waves have periods smaller than the acoustic cut-off period

$$P_A = \frac{4\pi c_S}{\gamma g} \,, \tag{4}$$

where $c_{\rm S}$ is the sound speed, g the acceleration due to gravity and $\gamma = 5/3$ the ratio of specific heats. Pulsational waves have periods $P \geq P_{\rm A}$. Typical values for the acoustic cut-off period for the Sun ($g = 2.74 \times 10^4$ cm s^{-2}, $c_{\rm S} = 7$ km s^{-1}) are $P_{\rm A} \approx 190$ s and for Arcturus ($g = 50$ cm s^{-2}, $c_{\rm S} = 6$ km s^{-1}) $P_{\rm A} \approx 1.5 \times 10^5$ s.

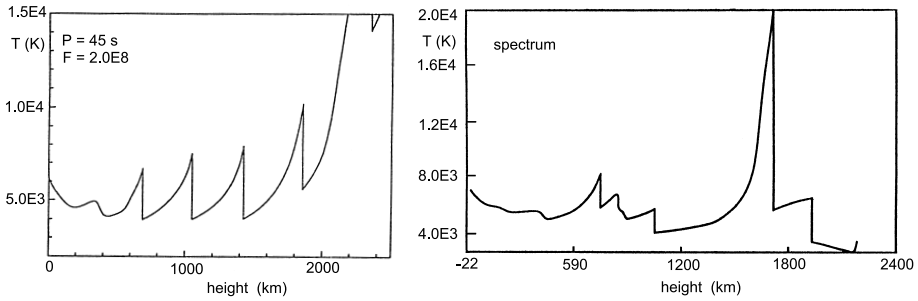

Fig. 2. Left: monochromatic, radiatively damped acoustic wave with period $P = 45$ s and initial energy flux $F_{\rm A} = 2 \times 10^8$ erg cm^{-2} s^{-1}. Right: propagating acoustic wave spectrum of the same initial energy

For *late-type stars* of spectral type F to M, acoustic waves are generated by turbulent velocity fluctuations near the top boundary of the stellar convection zones. The development of acoustic waves into shock waves is shown in Fig. 2. The left panel of this figure shows a calculation of a monochromatic, radiatively damped acoustic wave of period $P = 45$ s and initial energy flux $F_{\rm A} = 2 \times 10^8$

erg cm^{-2} s^{-1}. It is seen that the wave grows from a small amplitude up to a point where sawtooth shocks form which attain a limiting strength. This limiting strength for a given star depends only on the wave period (larger periods give stronger shocks). Also shown in Fig. 2 (right panel) is a calculation with an acoustic spectrum. Here shocks of different strengths are generated and one has the tendency that strong shocks eat up the weak shocks.

In *early-type stars* of spectral type O to A, where surface convection zones are absent, it is the intense radiation field of these stars which generates acoustic disturbances and amplifies them to strong shocks. This mechanism works as follows (Fig. 3). Consider a gas blob in the outer atmosphere of an early-type star. The line-opacity κ_ν as function of frequency ν of the outer atmosphere at rest is shown dashed in Fig. 3. Also shown is the intensity I_ν of the photospheric stellar radiation field which has an absorption line at that frequency. If by chance the gas blob acquires a slight outward velocity, then relative to the dashed profile, its line-opacity κ_ν (solid) is Doppler shifted towards the violet and photons from the violet wing of the stellar absorption line get absorbed in the blob, imparting more momentum and thus accelerating it even more (Fig. 3). This results in a line-opacity κ_ν shifted further out of the region of the photospheric absorption line, where additional photons accelerate the blob, etc. This process is called *radiative instability* and results in a powerful acceleration of gas blobs which leads to the formation of strong shocks with X-ray emitting post-shock regions and intense local heating leading to the coronal emission of these early-type stars.

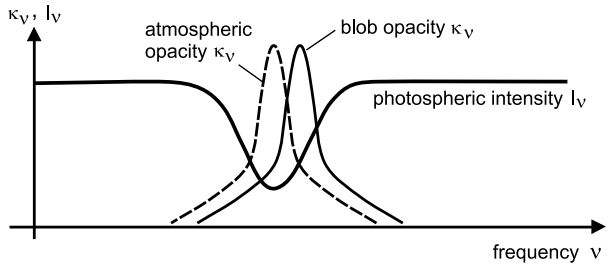

Fig. 3. Radiative instability for an accelerating gas blob in an intense radiation field

The other hydrodynamic heating mechanism is *pulsational waves*. Pulsational waves are prominent in Mira-star pulsations, but also in other late-type giants. These pulsations are generated by the *κ-mechanism*. The κ-mechanism (here κ refers to the opacity) functions similarly as the internal combustion engine in motorcars (see Fig. 4). In the internal combustion engine a reactive gas mixture is compressed in a pulsational motion and is ignited at the moment of strongest compression, resulting in a violent decompression. The timing of the ignition ensures that the pulsational motion is amplified. In the κ-mechanism the opacity of stellar envelope material increases (due to the adiabatic temperature and

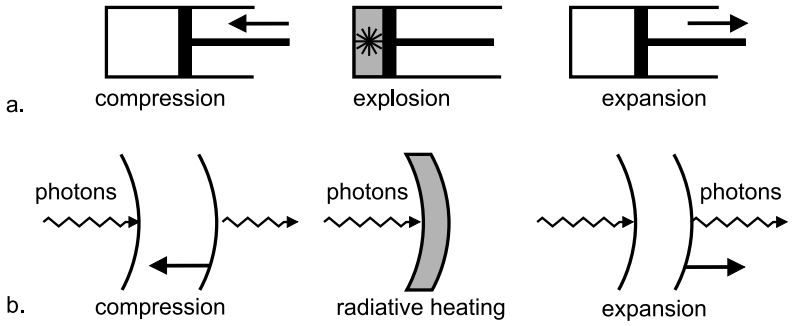

Fig. 4. (**a.**) Generation of pulsation by a gasoline engine, (**b.**) by the κ-mechanism

pressure increase) when the star contracts in a pulsational motion. The opacity increase leads to an increased absorption of radiation energy and thus to a large heat input into the contracted envelope layers. The overheated envelope layer subsequently reacts by rapid expansion, thus driving the pulsation. These pulsational waves propagate to the outer stellar atmosphere where they form shocks.

This and related processes, also with different drivers (e.g., the ϵ-mechanism where the nuclear energy generation is enhanced, see e.g., Kippenhahn & Weigert 1990), work also for nonradial oscillations. Any process which kicks on the basic pulsational and vibrational modes of the outer stellar envelope belongs to the category of pulsational wave mechanisms. For the Sun the 3 min oscillation is such an example of a basic resonance which is generated by transient events produced in the convection zone (3 min shock waves). Unfortunately, a systematic study of this heating mechanism for late-type stars is missing at the present time.

4 Magnetic Heating Mechanisms

It is observationally well established that isolated strong vertical magnetic fields (flux tubes) exist outside sunspots, particularly at the boundaries of supergranulation cells (e.g., Solanki 1993; Stenflo 1994; Schrijver & Zwaan 2000), and there they give rise to the chromospheric network emission in the chromospheric spectral lines. It is found that the cross-section of the magnetic flux tubes increases with height (see Hasan, this volume). At an altitude of about 1500 km the individual flux tubes fill out the entire available space and form the *magnetic canopy*. In the corona the field strength is $B \approx 10$–100 G. At the surface of the Sun the field strength in an isolated flux tube of the chromospheric network is $B \approx 1500$ G. One has horizontal pressure balance

$$p_i + \frac{B^2}{8\pi} = p_e \ , \tag{5}$$

where p_i is the gas pressure inside the flux tube and p_e the gas pressure in the non-magnetic region outside. At the solar surface at $z = 0$ one finds $p_\mathrm{e} = 1.2\times10^5$ dyn cm^{-2} in the Vernazza, Avrett & Loeser (1981) model C. If the tube were empty, that is, $p_\mathrm{i} = 0$, one would have $B = B_\mathrm{eq} = \sqrt{8\pi p_\mathrm{e}} = 1740\,\mathrm{G}$. This is called *equipartition field strength*. Actually the tube is not empty but has a gas pressure of about 1/3 to 1/6 of the outside pressure.

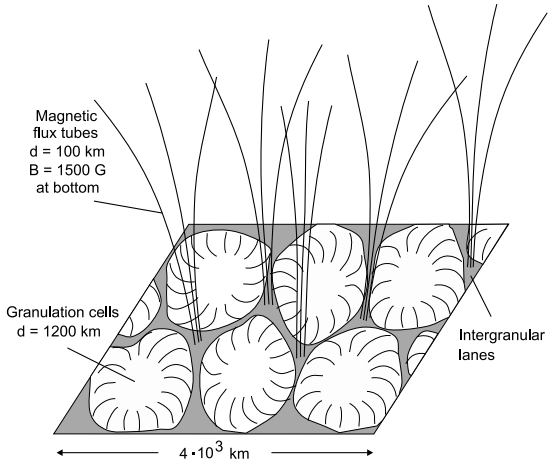

Fig. 5. Surface region of the Sun with granulation cells and magnetic flux tubes

For a discussion of the magnetic heating mechanisms consider a surface region on the Sun (Fig. 5). It is seen that the granulation flows, which are produced by rising turbulent gas bubbles in the convection zone, concentrate the magnetic fields into magnetic flux tubes in the intergranular lanes, where the gas flows back into the Sun. This flow is not laminar, and as it converges from a large area to the downflow region and because the Sun rotates, the flow experiences Coriolis forces and generates tornados (Fig. 6). A magnetic flux tube therefore sits in the centre of a tornado of downflowing gas. As the flows are turbulent there is a lot of squeezing, shaking and twisting of the flux tubes. These external perturbations generate three types of magnetohydrodynamic (MHD) wave modes (see Fig. 7). The squeezing produces *longitudinal MHD waves*, the shaking *transverse Alfvén waves*, and the twisting by turbulent cyclonic flows *torsional Alfvén waves*. Longitudinal tube waves cause cross-sectional variations of the tube, they are essentially acoustic tube waves. Because of this similarity they dissipate via shocks. The transverse and torsional Alfvén waves do not show a cross-sectional variation of the tube. In principle, the transverse and torsional waves can also form shocks (see Figs. 9, 10) but usually they are more difficult to dissipate (see e.g., Narain & Ulmschneider 1990, 1996).

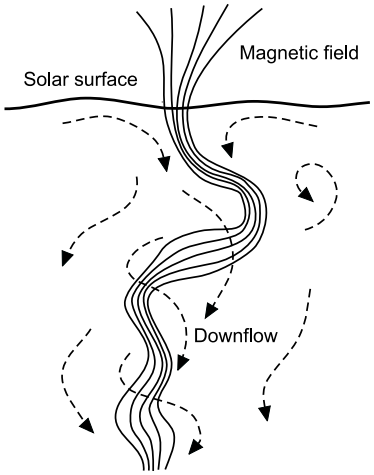

Fig. 6. Cyclonic turbulent downflows generate longitudinal, transverse and torsional MHD waves, modified after Parker (1981). The squeezing of the field lines produces longitudinal waves, the shaking transverse waves and the twisting torsional waves

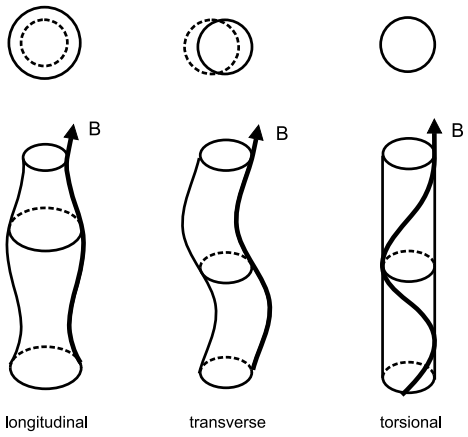

Fig. 7. The three possible wave modes in magnetic flux tubes. Cross-sections are shown at the top

A typical time scale is the Alfvén transit time $t_{\rm A}$:

$$t_A = \frac{l_\parallel}{c_A} = l_\parallel \frac{\sqrt{4\pi\rho}}{B} \,, \tag{6}$$

where $l_\parallel$ is the length of a magnetic loop or flux tube and $c_{\rm A}$ is the Alfvén speed. The magnetic waves are generated by *rapid* ($t << t_{\rm A}$) velocity fluctuations outside the tube. These fluctuations are produced in the convection zone, but also by sudden events (see Sect. 4.10). Above the canopy the waves encounter a more

or less homogeneous medium and other wave modes, *fast* and *slow mode* MHD waves are possible.

If the motions of the convection zone are *slow* ($t >> t_A$), then instead of waves, stressed magnetic structures are built up which contain a large amount of energy. Here often magnetic fields of opposite polarity are brought together and form current sheets. The energy of the stressed fields is then released by *reconnection*, where the field lines break open and reconnect in such a way that the field geometry afterwards is simpler. These reconnection processes usually occur suddenly like in a *flare* where the magnetic field energy of a large spatial region is released in seconds. Smaller reconnection events are called *microflares* (see Sect. 4.10). The local release of energy generates waves in turn. However, same as for waves the ultimate source of the DC-heating mechanism is the convection zone.

Let us now discuss the magnetic heating processes in detail.

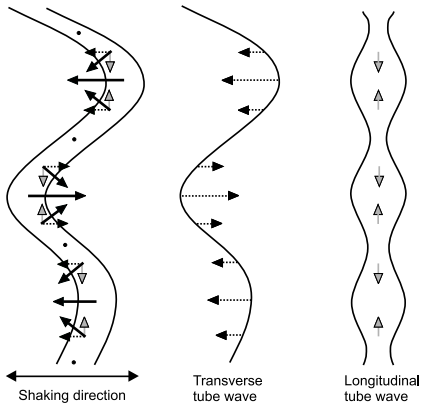

Fig. 8. Mode-coupling between transverse and longitudinal waves which results from the shaking of the flux tube

4.1 Mode-coupling

This mechanism is not a heating process by itself, but converts wave modes, which are difficult to dissipate by non-linear coupling into other modes, where the dissipation is more readily achieved. Typical cases are the conversion of transverse or torsional Alfvén waves into acoustic-like longitudinal tube waves which dissipate their energy by shock heating. Figure 8 shows an example of such a process when a magnetic flux tube is shaken. It is seen that the magnetic tension force which is directed towards the centre of curvature can be split into longitudinal and transverse components. The longitudinal force components act to compress and expand the gas in the tube such that a longitudinal wave of twice the frequency is generated.

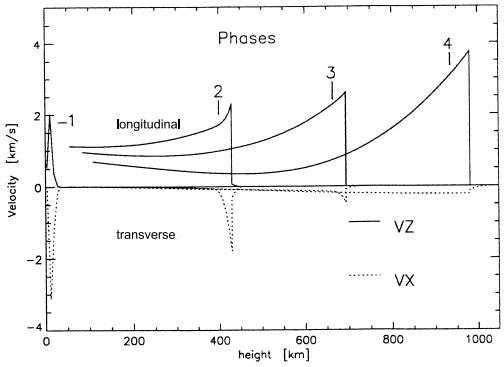

Fig. 9. Longitudinal wave pulse and shock generated by mode-coupling from a transverse wave pulse, after Zhugzhda, Bromm & Ulmschneider (1995). Different wave phases are labelled 1 to 4

Mode-coupling is particularly efficient when the transverse waves are very stochastic in nature as is expected from observation (Muller et al. 1994) and from wave generation calculations (e.g., Musielak & Ulmschneider 2001). Figure 9 (after Zhugzhda, Bromm & Ulmschneider 1995) shows the generation and development of a longitudinal shock wave pulse produced by mode-coupling from a transverse wave pulse. While the propagation speeds of the transverse and longitudinal waves are very different these authors find that when the shocks appear, both the transverse shocks (also called kink shocks) and longitudinal shocks form at the same height and subsequently propagate with a common speed. This indicates strong mode-coupling.

A similar process of mode-coupling occurs when torsional wave pulses propagate (Hollweg, Jackson & Galloway 1982). Figure 10a shows the propagation of various torsional wave pulses. The longitudinal waves generated by mode-coupling are displayed in Fig. 10b. It is seen that the torsional shocks (also called switch-on shocks) and longitudinal shocks form at the same height and subsequently propagate with a common speed indicating strong mode-coupling. These calculations have to be taken with some caution because it is not well known whether the thin flux tube approximation describes these situations well. Three-dimensional time-dependent work by Ziegler & Ulmschneider (1997) on swaying magnetic flux tubes in the solar atmosphere shows that there is extensive leakage of the transverse wave energy into the outside medium. Thus the true magnitude of the longitudinal wave energy generation by mode-coupling is presently not well determined.

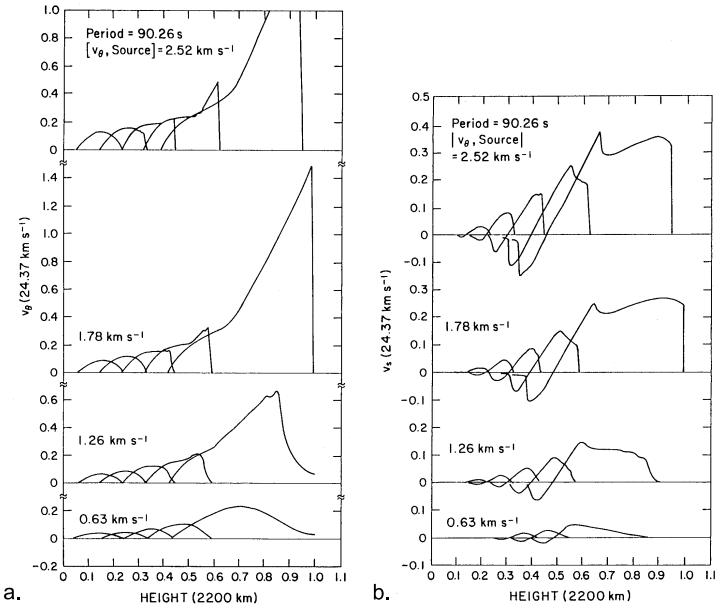

Fig. 10. Longitudinal waves and shocks generated by mode-coupling from torsional wave pulses. Different wave phases are indicated. (**a.**) propagation of torsional wave pulses of various initial amplitudes, (**b.**) corresponding longitudinal waves, after Hollweg, Jackson & Galloway (1982)

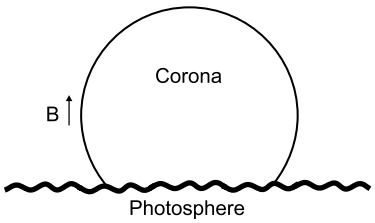

Fig. 11. Resonance heating in coronal loops

4.2 Resonance Heating

Resonance heating occurs, when upon reflection of Alfvén waves at the two foot points of the coronal loops, one has constructive interference (see Fig. 11). For a given loop length $l_\parallel$ and Alfvén speed c_A, resonance occurs, when the wave period is $mP = 2l_\parallel/c_\mathrm{A}$, m being a positive integer. Waves which fulfill the resonance condition are trapped and after many reflections are dissipated by Joule-, thermal conductive or viscous heating.

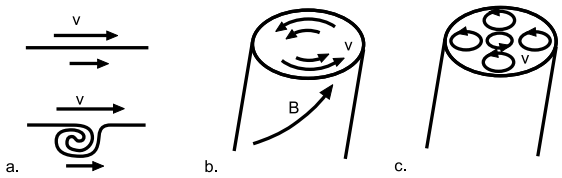

Fig. 12. Turbulent heating in magnetic flux tubes

4.3 Turbulent Heating

In a turbulent flow field with high Reynolds number there are bubbles of all sizes. The energy usually is put into the largest bubbles. Because of the large inertial forces, the moving big bubbles are ripped apart into smaller bubbles, and these in turn into still smaller ones etc. This process is called turbulent cascade. A turbulent flow field can be described by three characteristic quantities, density ρ, bubble size $l_\mathrm{k} = 2\pi/k$, and the mean velocity u_k of such bubbles. k is the wavenumber. It is easily seen, that from these three quantities only one combination for a heating rate can be formed

$$\Phi_k = \rho \frac{u_k^3}{l_k} \qquad \left[\frac{\mathrm{erg}}{\mathrm{cm}^3\,\mathrm{s}}\right] . \tag{7}$$

If there are no other losses, such as radiation, all the energy which is put in at the largest bubbles must reappear in the smaller bubbles etc. Thus if $k1, k2, \ldots$ represents a series of smaller and smaller bubbles one must have $\Phi_{\mathrm{k}1} = \Phi_{\mathrm{k}2} = \cdots = \mathrm{const}$. This implies

$$u_k \sim l_k^{1/3} , \tag{8}$$

which is the *Kolmogorov law*. The range $l_{\mathrm{k}1}, \ldots, l_{\mathrm{k}n}$ of validity of this law is called the *inertial range*. Consider what happens if l_k becomes very small. The viscous heating rate is given by $\Phi_\mathrm{V} = \eta_\mathrm{vis}(du/dl)^2 \approx \eta_\mathrm{vis} u_\mathrm{k}^2/l_\mathrm{k}^2 \approx \eta_\mathrm{vis} l_\mathrm{k}^{-4/3}$, which goes to infinity for $l_\mathrm{k} \to 0$. Here η_vis is the coefficient of viscosity. Thus at some small enough scale, viscous heating sets in and the inertial range ends. It is seen that turbulent heating lives from the formation of small scales. One can visualise the process as follows. Because of the continuous splitting of bubbles into smaller sizes, with the velocities decreasing much less rapidly, one eventually has close encounters of very small bubbles with large velocity differences where viscous heating dominates.

As the fluctuations generated in the turbulent convection zone produce acoustic and MHD waves it is of interest to deduce from the inertial range an estimate of the frequency range of the generated waves. If $k_0 \approx 2\pi/H$ is the wavenumber of the scale where the energy is put into the turbulence, with H being the scale height, we have for the size l_k of the smallest bubble (where viscosity ends the cascade) $\eta_\mathrm{vis} u_\mathrm{k}^2/l_\mathrm{k}^2 = \rho u_{\mathrm{k}_0}^3/l_{\mathrm{k}_0}$ and $u_\mathrm{k}^3/l_\mathrm{k} = u_{\mathrm{k}_0}^3/l_{\mathrm{k}_0}$. From this we obtain

$$l_k = \left(\frac{\eta_\mathrm{vis} l_{\mathrm{k}_0}^{1/3}}{\rho u_{\mathrm{k}_0}}\right)^{3/4} . \tag{9}$$

With $l_{k_0} = H = 150\,\mathrm{km}$, $u_{k_0} = 1\ \mathrm{km\ s^{-1}}$, $\rho = 3 \times 10^{-7}\ \mathrm{g\ cm^{-3}}$, $\eta_{vis} = 5 \times 10^{-4}$ dyn s $\mathrm{cm^{-2}}$, one finds $l_k = 2.9\,\mathrm{cm}$ as well as $u_k = 290\ \mathrm{cm\ s^{-1}}$ and derives a maximum frequency of $\nu_k = u_k/l_k = 100\,\mathrm{Hz}$ or a period of $P = 1/100\,\mathrm{s}$. This estimate is somewhat idealised as small bubbles become transparent to radiation. In this case the temperature excess, which drives the convection, is exchanged directly via radiation. Thus it is expected that the optical depth limits the bubble size. Assuming that the smallest bubble has an optical depth of $\tau = l_k \kappa = 0.1$, where

$$\frac{\kappa}{\rho} = 1.38 \times 10^{-23} p^{0.738} T^5 \quad \mathrm{cm^2\ g^{-1}}\ , \tag{10}$$

is the gray H^- opacity, $T = 8320\,\mathrm{K}$ the temperature and $p = 1.8 \times 10^5$ dyn $\mathrm{cm^{-2}}$ the gas pressure, one finds $l_k = 6.3 \times 10^4$ cm, $u_k = 1.6 \times 10^4\ \mathrm{cm\ s^{-1}}$, $\nu_k = 0.25\,\mathrm{Hz}$ and $P = 3.9\,\mathrm{s}$ for the smallest bubble.

So far we have discussed turbulent heating in a non-magnetic environment. When there is a magnetic flux tube one has to take into account the tube geometry, the frozen-in condition and the MHD wave modes. Fig. 12 shows how the turbulent dissipation of a torsional Alfvén wave is pictured (after Heyvaerts & Priest 1983; Hollweg 1983). Shearing motions in azimuthal direction generate closed magnetic loops (similarly to the growth of Kelvin–Helmholtz type instabilities) over the tube cross-section, which decay into smaller tubes etc. and are ultimately dissipated by reconnection.

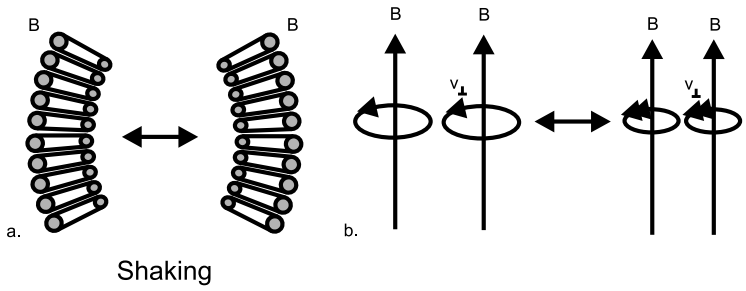

Fig. 13. Compressional viscous heating in helical fields. (**a.**) Cross-section (gray) of a magnetic flux tube with greatly exaggerated winding. The shaking of the spring leads to compressions and expansions of the tube. (**b.**) The field strength changes from the cross-section variations affect the gyro-frequency

4.4 Compressional Viscous Heating

Compressional viscous heating, proposed by Strauss (1991), is a very promising mechanism for coronal regions where the collision rate becomes small and the gyro-frequency gets much larger than the collision-frequency. In the presence of magnetic fields the particles have no restriction moving parallel to the magnetic field **B**, but cannot move freely perpendicular to it. In this direction when there

are few collisions, Lorentz forces cause them to orbit around the field lines with the gyro-frequency $\Omega_{\rm L} = qB/mc$, where c is the light velocity, q the charge and m the mass of the gyrating particle.

Swaying an axial magnetic flux tube sideways with velocity $\mathbf{v}_\perp$ results in a transverse Alfvén wave which is incompressible ($\boldsymbol{\nabla}\cdot\mathbf{v}_\perp = 0$) to first order. This is different for tubes with helicity, where one has $\boldsymbol{\nabla}\cdot\mathbf{v}_\perp \approx \dot{\rho}/\rho$ (see Fig. 13). With an increase of the density, the magnetic field is compressed and the gyro-frequency increased. Gyrating around the field lines more quickly in a narrower space, the ions collide more readily with each other, and generate velocity components in other directions as well, which constitutes the heating process.

4.5 Ion-cyclotron Resonance Heating

This type of damping also occurs at coronal heights, where due to the low density the collision rate becomes small. Due to the decreasing magnetic field strength B with height, high frequency torsional or transverse Alfvén wave propagating along the field lines will come to regions where the wave frequency becomes equal to the gyro-frequency $\Omega_{\rm L}$ of protons and ions like e.g., O^{5+}. Here ion-cyclotron resonance heating occurs. The concerted gyrations of the ions caused by the wave action leads to intersections of the orbits. This results in collisions which convert the wave energy into random motions, constituting the heating process. Ion-cyclotron resonance heating has been proposed e.g., by Tu & Marsch (1997, 2001a, 2001b) to explain the different types of parallel and perpendicular temperatures (with respect to the magnetic field $\mathbf{B}$) of protons, alpha particles and oxygen ions and their distribution with distance from the Sun in the solar wind.

4.6 Landau Damping

Landau damping is a third damping process which occurs at coronal heights where the collision rates are small. As Chen (1974) has explained, this mechanism is analogous to surfing on ocean waves (see Fig. 14a). When surfing, a surfboard rider launches himself in propagation direction into the steepening part of an incoming wave and gets further accelerated by this wave. In Landau damping, the propagating wave accelerates gas particles which, due to their particle distribution function, happen to have similar direction and speed as the wave. Because a distribution function normally has many more slower particles than faster ones (Fig. 14b), the wave looses energy to accelerate the slower particles (solid line in Fig. 14c). This gained energy is eventually shared with other particles in the process to reestablish the distribution function (dashed line in Fig. 14c), which constitutes the heating mechanism.

4.7 Resonant Absorption

In the process of resonant absorption one considers magnetoacoustic surface waves in a magnetic field $\mathbf{B}$ which points in z-direction, and varies from $\mathbf{B}_1$ to

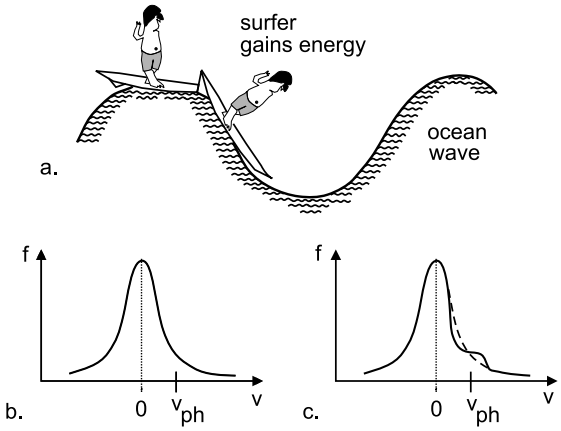

Fig. 14. Landau damping and the analogy to surfing. (**a.**) Surfing the ocean waves. (**b.**) Particle distribution function. (**c.**) Around its phase speed the wave modifies the distribution function

$\mathbf{B}_2$ in x-direction (see Fig. 15a). The surface wave, with its field perturbation $\delta B = B'_x$ in x-direction, has a phase speed $v_{\rm ph} = ((B_1^2 + B_2^2)/(4\pi(\rho_1 + \rho_2))^{1/2}$ such that at an intermediate position x_o, the phase speed becomes equal to the local Alfvén speed $c_{\rm Ao} = B(x_o)/\sqrt{4\pi\rho(x_o)}$. In Fig. 15b consider the wave fronts of the peak (solid) and trough (dotted) of a surface wave. Because to the right of x_o, the Alfvén speed is larger and to the left smaller, the wave fronts at a later time get tilted relative to the phase propagating with speed $c_{\rm Ao}$ (Fig. 15c). At a still later time (Fig. 15d) the wave fronts get tilted even further and approach each other closely at the position x_o. This leads to small scales and intense heating by reconnection at that field line.

4.8 Phase-mixing

For phase-mixing (Fig. 16) one considers a magnetic field geometry similar to that in Fig. 15, however, the field perturbation $\delta B = B'_y$ of the wave is now in y-direction, perpendicular to the x- and z-directions. As the Alfvén speeds of two closely adjacent regions x_0 and x_1 are different, it is seen that after propagating some distance Δz, the fields $B'_y(x_0)$ and $B'_y(x_1)$ will be very different, leading to a current sheet and strong dissipation. Here again it is the appearance of small scale structures which leads to the dissipation.

4.9 Reconnection in Current Sheets

Let us now discuss DC-mechanisms. In Fig. 17 the magnetic flux tube bundle which represents a closed coronal loop is plotted such that the two ends of the loop, which both originate in the photosphere, are displayed on the top and bottom of the figure. This way the minimum energy configuration, where the field

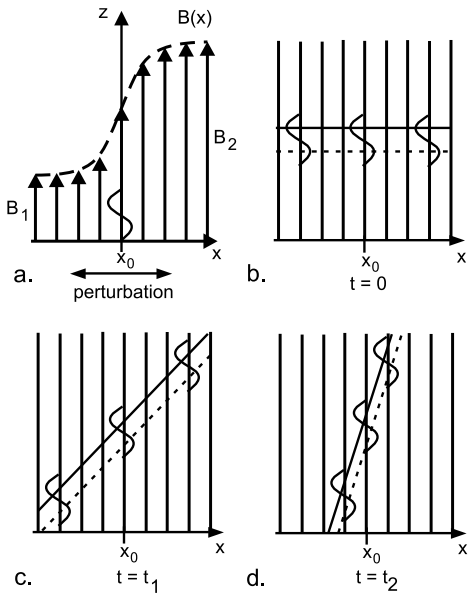

Fig. 15. Resonant absorption. In a field pointing in z-direction, where the field strength varies in x-direction. (**a.**) resonant absorption of a surface wave, (**b.**) wave fronts at time $t = 0$, (**c.**) and (**d.**) at later times t_1 and t_2

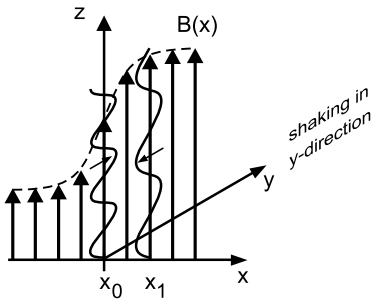

Fig. 16. Phase-mixing of a surface wave (shaking in y-direction)

lines are all straight and parallel, can be shown in the left panel. As the granular flows in the photosphere will displace the foot points of the individual flux tubes of the bundle, they get entwined such that after a while a complicated mesh of flux tubes results (right panel). This braided mesh has more stored energy than the minimum energy configuration and there is no chance that the flows will ever precisely reverse such that the minimum energy configuration reappears. On the contrary, the continuing motions will store more and more energy in the magnetic field until this can no longer go on.

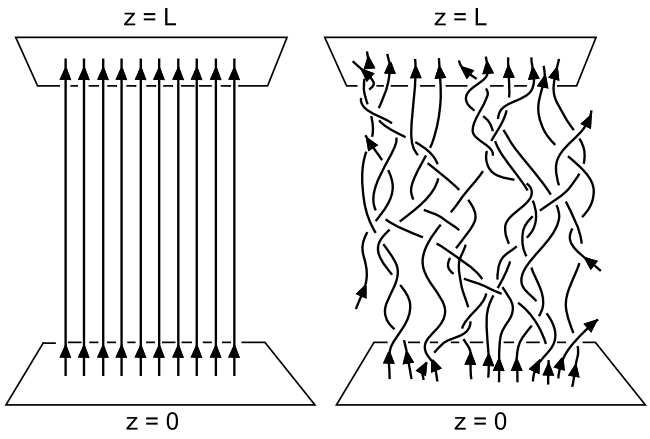

Fig. 17. Left: Magnetic fields in coronal loops, initial axial field. Right: tangled fields after considerable foot point motions, after Parker (1991)

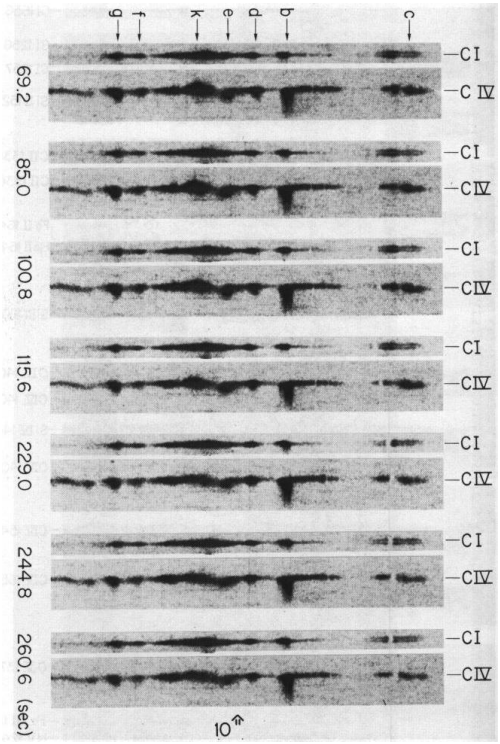

Fig. 18. Various outbreaks of C IV emission from high-velocity turbulent events in the transition layer observed on the Sun, after Brueckner (1981)

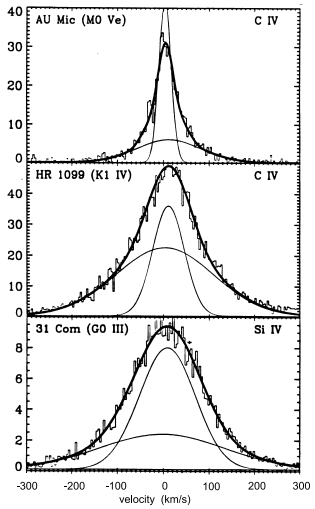

Fig. 19. Surface fluxes in transition layer lines (in 10^4 erg cm^{-2} s^{-1} Å^{-1}) of giants and main sequence stars, after Wood, Linsky & Ayres (1997)

At many locations in the web of field lines, oppositely directed fields occur, giving rise to local current sheets, which by reconnection (in the form of numerous microflares) release the magnetic field energy (see also Narain & Ulmschneider 1990, 1996, and recently Mitra-Kraev & Benz 2001). The energy is dissipated both directly and via the generation of waves and turbulence. Note that similarly to the wave mechanisms, reconnection happens in small scale regions.

Such small scale reconnective events of different magnitude have been observed on the Sun by Brueckner (1981) (see Fig. 18) and Brueckner & Bartoe (1983) as sudden velocity shifts in the C IV ($T \approx 10^5$ K) transition layer line with velocities of 250 km s^{-1} and even 400 km s^{-1}. These sudden velocity shifts have been called turbulent events and high velocity jets.

The question whether microflares are a significant coronal heating mechanism and what its importance is as compared to wave heating (DC- versus AC-heating) has also been studied by Wood, Linsky & Ayres (1997) by observing C IV and Si IV transition layer lines on stars other than the Sun (see Fig. 19).

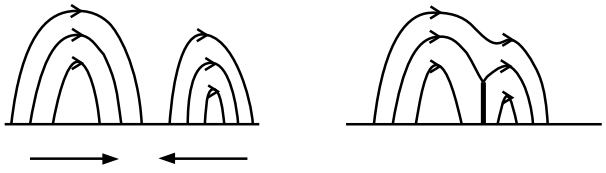

Fig. 20. Formation of current sheets in arcade systems, after Priest (1991)

They found that the total line profile can be explained as a combination of a broad component, attributed to microflares, and a narrow component attributed to wave heating.

Another example of current sheet formation and DC-heating is seen in Fig. 20, after Priest (1991). It shows arcade systems, which from slow motions get laterally compressed and develop a current sheet. Here oppositely directed fields reconnect. Similar systems of approaching magnetic elements of opposite polarity and large scale field annihilation are thought to be responsible for the heating of X-ray bright points.

5 Acoustic Energy Generation

After discussing the extensive list of proposed heating mechanisms we now ask which of these mechanisms are the important ones for chromospheres and coronae. Of most mechanisms we already know that they work in terrestrial laboratory settings and therefore should also work on the Sun, given the right situation and magnetic field geometry. Due to the large density decrease from the photosphere to the corona the heating requirements as function of height are very different and therefore some of the mechanisms will be more important than others.

In addition there are variations due to the magnetic field geometry. Magnetic surface waves, for instance, dissipate energy which propagates through a ring shaped cross-section around the magnetic flux tube. The heating per volume of solar atmosphere is probably much less efficiently done by surface waves than by body waves such as longitudinal tube waves or transverse and torsional Alfvén waves which employ the entire tube cross-section for transportation and dissipation of the energy. Finally, the importance of a heating mechanism depends on how effectively it can be produced in the convection zone. One thus has the tedious task to investigate each of the proposed heating mechanisms in detail in order to understand how much energy it carries and where and how it dissipates this energy.

Ideally the identification problem could be solved by a full scale simulation of the convection zone including the magnetic field together with the generation of the different wave types and the formation of current sheets (like e.g., in

Fig. 17). In such a simulation one would have to compute the motions and development of the physical variables on very different geometrical scales, from the supergranulation size of about 50 000 km down to about a few m where the shock dissipation and current sheet dissipation happens. While undoubtedly such simulations will be attempted in the future they are at the moment beyond our numerical capabilities. So far energy generation calculations are available only for a few mechanisms, all of them waves, and of the waves only for the three types: acoustic waves, longitudinal MHD waves and transverse Alfvén waves.

Let us concentrate on those heating mechanisms where the mechanical energy generation can be computed and start with the hydrodynamic mechanisms. To calculate acoustic fluxes of the Sun and other stars one must first compute a

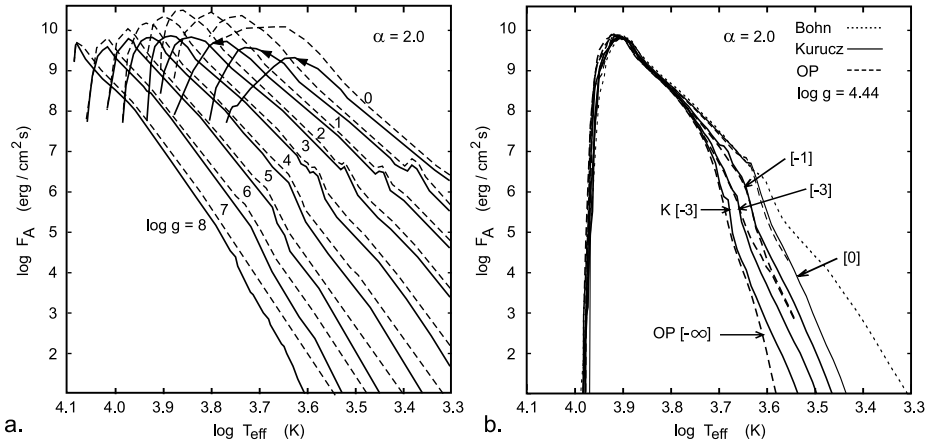

Fig. 21. Acoustic fluxes $F_{\rm A}$ for stars versus $T_{\rm eff}$, (**a.**) for given $\log g$ and $\alpha = 2.0$ (*solid*), the fluxes using the Lighthill formula are shown *dashed*, after Ulmschneider, Theurer & Musielak (1996), (**b.**) for $\log g = 4.44$ and different metal abundances $[Z_{\rm m}]$, after Ulmschneider et al. (1999). In **b.** Bohn opacities are shown *dotted*, Kurucz opacities *solid* and OP opacities *dashed*

convection zone model. As convection zones do not depend on rotation, such a model can be computed by specifying only three parameters: $T_{\rm eff}$, g and $Z_{\rm m}$. Actually, because the convection zone calculations use the *mixing-length theory*, a fourth parameter, the mixing-length parameter α, has to be specified. This dimensionless quantity α is the ratio of the mixing-length L to the scale height H and from solar and stellar observations one typically has $\alpha \approx 2.0$ (for references about the choice of α see Theurer, Ulmschneider & Kalkofen 1997). However, α is not a basic parameter, and in the future, numerical convection zone calculations will specify its precise value and replace the mixing-length theory altogether.

With density ρ, convective velocity u, sound speed $c_{\rm S}$ and scale height $H = \Re T/\mu g$ versus height z, provided by the convection zone models, acoustic fluxes $F_{\rm A}$ can be computed using either the simple so called *Lighthill-* or *Lighthill–Proudmann formula*, or the more elaborate Lighthill–Stein theory (Musielak et al. 1994). Here $\Re$ is the universal gas constant and μ the mean molecular weight. Figure 21a shows acoustic fluxes for stars with (solar) population I abundances ($[Z_{\rm m}] = 0$ and $\alpha = 2.0$) for a wide range of late-type stars after Ulmschneider, Theurer & Musielak (1996), while Fig. 21b displays acoustic fluxes for stars with 1/1, 1/10, 1/100 and 1/1000 solar metal abundances ($Z_{\rm m} = [0], [-1], [-2], [-3]$ and $\alpha = 2.0$) after Ulmschneider et al. (1999).

Both the Lighthill formula and the Lighthill–Stein theory use the experimentally and theoretically well established energy distribution of free turbulence described by a Kolmogorov energy spectrum. Lighthill and Proudman derived a

simple formula

$$F_A = \int 38 \frac{\rho u^8}{c_S^5 H} \, \mathrm{d}z \, , \tag{11}$$

with the famous u^8-dependence for *quadrupole sound generation*. This u^8-law has been successfully reproduced in terrestrial experiments as shown in Fig. 22. Also one finds in Fig. 21a that the total acoustic fluxes using the elaborate Lighthill–Stein theory are surprisingly close to values given by the Lighthill formula which is due to the similar Kolmogorov energy spectrum used. Actually in the Lighthill–Stein theory a slightly different extended Kolmogorov spatial spectrum with a modified Gaussian frequency factor (eKmG spectrum) has been employed (Musielak et al. 1994).

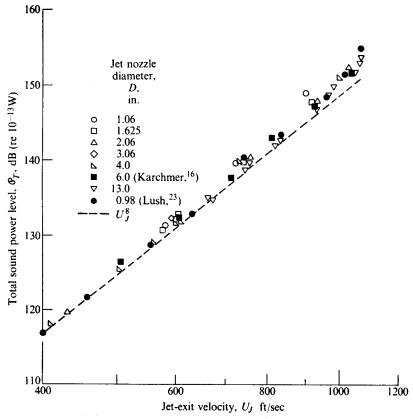

Fig. 22. Lighthill's u^8 power law in terrestrial applications, after Goldstein (1976)

In Fig. 21a one sees that the acoustic flux F_A rises rapidly with T_eff and g. This is explained from the fact that the convective velocity u increases when a star gets hotter and/or its gravity decreases. The large variation is due to the u^8-dependence. That F_A varies with metallicity (in Fig. 21b) is a consequence of the location of the top boundary of the convection zone in a star. That boundary is the layer where rising convective bubbles reach the stellar surface and radiate their temperature excess directly into space. In cool stars with large Z_m the opacity is large and thus the top of the convection zone lies at shallow layers where convection employs large velocities to transport the stellar flux σT_eff^4. For lower metal content the opacity decreases and the boundary moves to layers of higher density where the convective velocity is smaller. This explains why F_A decreases for lower Z_m. For hot stars the opacity is mainly due to hydrogen and not to metals and thus F_A does not vary with Z_m.

6 Theoretical Chromospheres

The Lighthill–Stein theory not only provides the total acoustic flux $F_{\rm A}$ (erg cm^{-2} s^{-1}) but also an acoustic frequency spectrum. For monochromatic calculations the maximum of this spectrum determines the wave period $P(s)$ which can be used together with $F_{\rm A}$ to compute the propagation of acoustic waves into the chromosphere (Buchholz, Ulmschneider & Cuntz 1998). For this computation one first needs an initial radiative equilibrium atmosphere model for the star, which depends on $T_{\rm eff}$, g and $Z_{\rm m}$. The wave calculation and the initial atmosphere computation both employ frequency-dependent radiation by the H^- continuum and single MgII k, CaII K and Lyα lines, taking into account departures from local thermodynamic equilibrium (NLTE). Multiplying the losses from single lines with scaling factors, the total chromospheric losses are simulated.

Wave calculations require an initial atmosphere model. This initial model is constructed by using a (time-independent) standard temperature correction procedure (Cuntz et al. 1999), from which one usually obtains an outwardly decreasing temperature profile. The time-dependent wave code introduces the acoustic wave in this model by applying a velocity perturbation at the lower boundary:

$$v = -v_0 \sin\left(\frac{2\pi}{P}t\right) \ , \tag{12}$$

where $v_0 = \sqrt{2F_{\rm A}/(\rho\ c_{\rm S})}$ is the wave amplitude, and the minus sign is taken to minimise switch-on effects. Switch-on effects are large transient events which occur when a numerical wave calculation is started and the initial atmosphere reacts strongly to the incoming wave. Here ρ is the density and $c_{\rm S}$ the sound speed at the bottom. One usually takes monochromatic waves instead of the full acoustic spectrum because of the greater simplicity of the computation and because the results can be more easily analysed.

Figure 23 shows a snapshot from a wave calculation for the Sun with $P = 45$ s and $F_{\rm A} = 1 \times 10^8$ erg cm^{-2} s^{-1}. The temperature profile of the initial atmosphere is labelled T_0. The snapshot is shown at a time where many waves have already gone through the atmosphere. It is seen that the wave at first has a rapid amplitude growth with height, and that near 500 km height shocks form, which quickly attain a saw tooth shape. For monochromatic waves the shocks reach a constant limiting strength (magnitude of the shock jump) which depends on the wave period. For small wave amplitudes the magnitude of the shock jump is directly proportional to the wave period. After shock formation the mean temperature (after time-averaging, (dash-dot-dash)) increases in outward direction and at about 2000 km rises rapidly. This temperature behaviour is called a *classical chromosphere*.

The reasons for the rapid rise at great height are the following. When a shock traverses a gas element, its temperature abruptly increases. Subsequently the temperature gradually decreases again due to radiative cooling. When the temperature jump has not been completely radiated away before the next shock

arrives, then the mean temperature in the gas element rises. Therefore, after a long time, a mean temperature is established in the gas element such that the heat brought by the temperature jump is exactly removed by radiative cooling until the next shock arrives, a state called dynamical equilibrium. Now at great height where the mean temperatures are high, the typical emitters Ca II, Mg II and H I get ionised to Ca III, Mg III and H II, respectively. By destroying the cooling mechanism the shock heating thus becomes unbalanced (heating catastrophe). The reaction of the atmosphere is that the temperature shoots up rapidly into the transition layer and corona.

To compare such theoretical chromospheres with observations one computes the line profiles of the Mg II h and k as well as Ca II H and K lines. Figure 24 shows the observed Ca II K line from the Utrecht solar atlas. Because the chromosphere is a very tenuous layer overlying the photosphere it is only visible as emission peaks in the line core. The inset of Fig. 24 indicates the terminology of the spectral features of the K line, the minima K_1, the emission peaks K_2 and the central absorption feature K_3.

The Ca II line profile mirrors the temperature profile of the atmosphere. This is seen in Fig. 25. The opacity, shown in Fig. 25b varies rapidly with frequency. From radiative transfer theory the monochromatic intensity at a wavelength difference $\Delta\lambda$ from line centre is equal to the source function (essentially the Planck function) at optical depth unity for that wavelength, that is, one has $\tau_\lambda = -\int \kappa_\lambda \, dz = 1$. Here z is the height in the atmosphere (Fig. 25) and κ_λ the opacity. At $\Delta\lambda = \pm 10$ Å the opacity is low and one can look into very deep layers of the star where one has high photospheric temperatures, and where one obtains high intensities in the wings of the line. At $\Delta\lambda = \pm 0.4$ Å one has much higher opacity and one can look only as far as the temperature minimum (K_1 in Fig. 24). There the Planck function is small and one gets a low intensity. Finally at $\Delta\lambda = \pm 0.2$ Å one has very high opacity and looks only as far as the

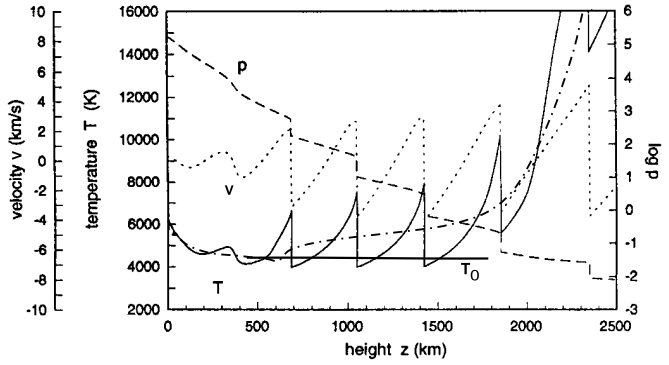

Fig. 23. Acoustic wave calculation. The velocity v, temperature T and $\log p$ in dyn cm^{-2} are shown as function of height z

chromosphere where the temperature is high and one gets a high intensity (K_2 in Fig. 24). This very nice mapping of the temperature profile onto the line profile breaks down in the innermost line core, where NLTE effects decouple the source function and thus intensity from the temperature distribution, which leads to the K_3 intensity dip at line centre (Fig. 24). From this it is clear that the emission cores of the Ca II, Mg II and Lyα lines are generated by a chromosphere.

Figure 26 shows wave calculations by Buchholz & Ulmschneider (1994) for three main-sequence stars of spectral type F0V, G5V and K5V. On basis of the theoretical chromosphere models the Ca II K and Mg II k lines were simulated (Fig. 26). Integrating the monochromatic fluxes in these emission cores, total chromospheric emission fluxes in these lines can be computed and compared with stellar observations as shown in Fig. 27. These observations (Rutten et al. 1991) measure the energy flux of the emission cores of the Ca II and Mg II lines and find that all late-type stars have at least a minimal core emission indicating a chromosphere. This empirically found lower envelope of stellar chromospheric emission is called *basal flux line* (heavy solid in Fig. 27). For the significance of the other lines in the figure see Rutten et al. (1991), and for more details on the basal flux line see also Fawzy et al. (2002b). Note that the basal flux line is found to be the same for main-sequence stars, giants and for stars with low metallicity. But there are also stars in Fig. 27 which show a much higher emission and therefore there also is an upper envelope called *saturation limit* at high chromospheric emission.

It is seen in Fig. 27 that the theoretical Ca II and Mg II fluxes agree quite well with the basal flux line. Note that the theoretical calculations are completely ab initio computations, based only on the three parameters $T_{\rm eff}$, g and $Z_{\rm m}$, and that there are only these three basic parameters through which acoustic energy generation in the stars can vary. Therefore, the agreement with the purely observational basal flux line not only for main-sequence stars (varying $T_{\rm eff}$), but

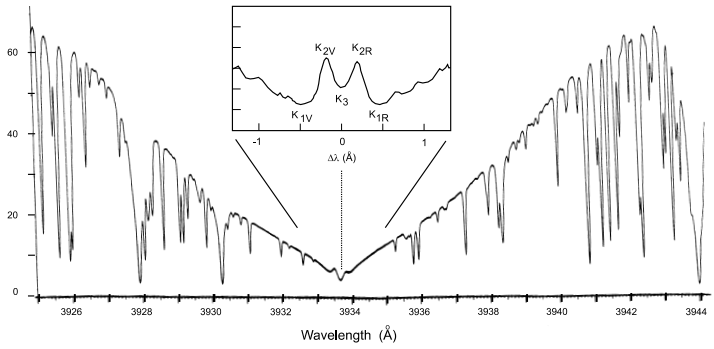

Fig. 24. Ca II K line profile from the Utrecht solar atlas, inset: terminology of the Ca II K core region

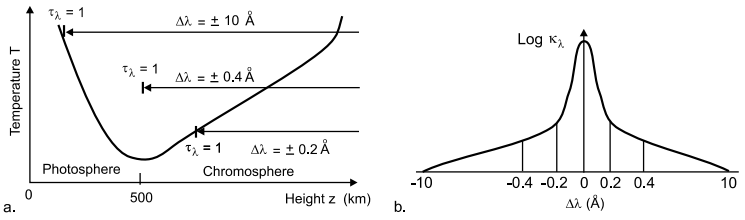

Fig. 25. Ca II line formation. (**a.**) temperature versus height, (**b.**) line opacity versus wavelength difference from line centre

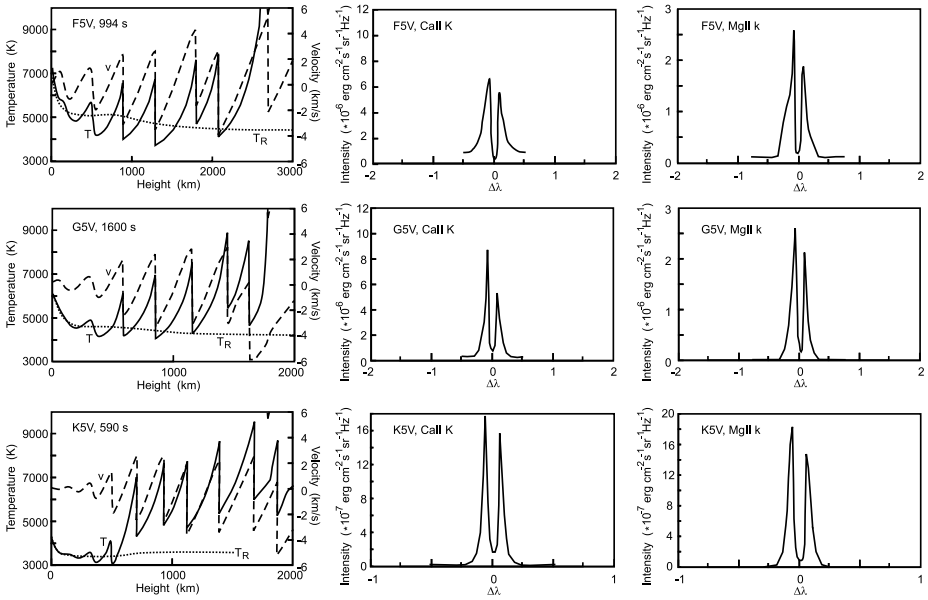

Fig. 26. Chromosphere models with acoustic shock waves (left panels), Ca II K line core profiles (middle panels) and Mg II k line core profiles (right panels) simulated for these chromosphere models for three different main sequence stars, after Buchholz & Ulmschneider (1994). $T_{\rm R}$ is the initial radiative equilibrium temperature distribution at the start of the calculation

also for giants (varying g) as well as low metallicity stars (varying $Z_{\rm m}$) suggests that *acoustic waves are the basic heating mechanism for stellar chromospheres.*

But the stars with emission fluxes higher than the basal flux need an additional (magnetic) heating mechanism. Indeed it is found that the chromospheric emission strongly depends on rotation and that the greater the rotation the higher is the chromospheric emission (rotation–emission correlation, see Fig. 45 below). As the dynamo mechanism depends on convection and rotation, the more rapid the star rotates, the greater is the magnetic flux that covers the star. The

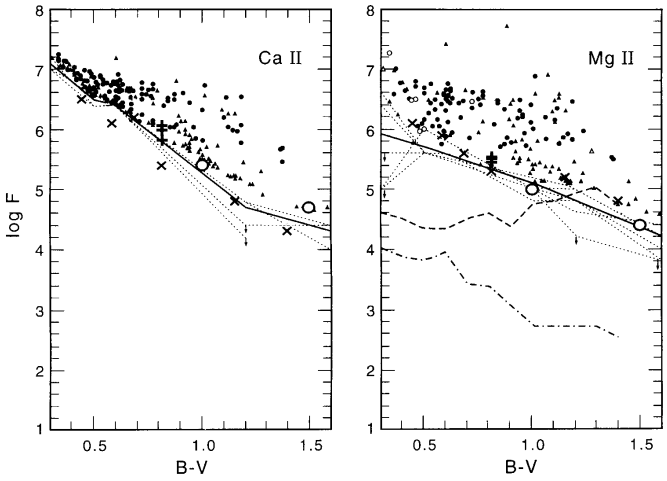

Fig. 27. Comparison of the chromospheric emission from acoustically heated theoretical chromosphere models with observations in Ca II and Mg II lines. (x) mark main-sequence stars of solar metal abundances, (o) giant stars of solar abundances, while (+) mark giants with 1/1, 1/10 and 1/100 solar metal abundances, after Cuntz, Rammacher & Ulmschneider (1994) and Buchholz, Ulmschneider & Cuntz (1998). The empirical basal flux line is marked heavy solid

chromospheric emission higher than the basal flux line thus involves the fourth basic stellar parameter $P_{\rm Rot}$.

7 Semi-empirical Chromosphere Models

Vernazza, Avrett & Loeser (1981) generated semi-empirical solar chromosphere models by selecting temperature distributions which optimally predict observed spectral features (mainly UV continua but also lines) and by assuming hydrostatic equilibrium to obtain the density and pressure distribution (see Fig. 28). Non-solar semi-empirical chromosphere models are based almost exclusively on the intensity profiles of the Ca II and Mg II lines. Examples of such models are shown in Fig. 29. Here in a first step with the stellar parameters $T_{\rm eff}$ and g, radiative and hydrostatic equilibrium photosphere models are computed (dashed in Fig. 29). Then in a second step the simulated Ca II K line profiles based on various outward temperature distributions (solid) are optimally fitted to the observed line wings.

It should be noted that all of these models, both semi-empirical and early theoretical models, in addition to an enhanced photospheric temperature distribution invariably show a classical chromosphere with a monotonic outwardly increasing temperature (Figs. 28, 29, 23). Clearly semi-empirical and theoretical models cannot fully agree, because for the semi-empirical modelling a smooth

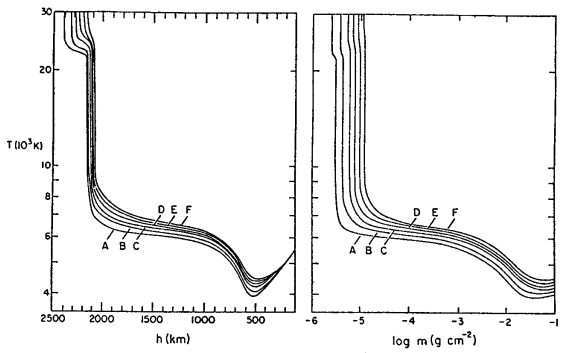

Fig. 28. Semi-empirical solar chromosphere models by Vernazza, Avrett & Loeser (1981)

monotonic temperature and emission distribution versus height is assumed, while in the theoretical calculations the temperature varies inhomogeneously with the radiation primarily concentrated in the hot regions behind the shocks. However, by time averaging, this emission is smoothed out such that it appears monotonic. This smoothing can also be thought as the result of a large number of independent shock wave propagations averaged over the wide expanse of the stellar surface.

Such wave effects can explain for instance why pure Ca II line semi-empirical models give lower temperatures than pure Mg II line models because the ultraviolet Mg II emission in the post shock region has a stronger temperature dependence than the Ca II emission. Aside of these effects, both semi-empirical and theoretical models agree reasonably well. However, this picture of classical chromospheres in the last few years has been challenged by Carlsson & Stein (1995) who argued that the time-dependence in the chromosphere is much more extreme than previously thought and that over most of its height the excess chromospheric emission is due to strong solitary waves which propagate over the outwardly decreasing radiative equilibrium temperature distribution.

8 Extremely Time-dependent Chromospheres

To firmly establish the presence of propagating acoustic waves which explain the observed time-dependent profile variations and phase relations of chromospheric lines, Carlsson & Stein (1994, 1997) employed a hydrodynamic code which incorporates the time-dependent treatment of the rate equations (which determine the populations of the energy levels), the hydrogen ionisation and the radiative transfer equations for H^-, hydrogen and various chromospheric lines (Ca II, Mg II). In order to decouple themselves from the uncertainties of the generation of acoustic waves in the convection zone, the authors decided to use observed velocity fluctuations in a low-lying Fe I line (at 3966.8 Å formed at a

height of about 250 km) observed by Lites, Rutten & Kalkofen (1993) as input for their wave code. The idea was to use an observed input and to simulate the perturbation caused by this wave input at greater height, and to explain the complicated line shifts and profile brightenings in the core of the Ca II H line at 3968 Å which was recorded simultaneously with the Fe line. This velocity input and its frequency spectrum is shown in Fig. 30.

The result of the simulation was impressive, as the authors were able to reproduce quite well the complicated time-dependent core behaviour of the Ca II H line which is formed at a height of about 1500 km. This showed that indeed propagating acoustic waves are essential for explaining the time-dependent behaviour of the chromosphere. The success of this simulation proved even more impressive when the frequency-dependent phase differences between velocity fluctuations in spectral lines originating from different heights were compared.

To explain these phase differences, we discuss the Doppler shift observations of Fleck & Deubner (1989). Figure 31 shows how at some point on the slit of a spectrograph (and thus at a given spatial location on the Sun) the Doppler shifts relative to the rest frequency ν_0 of two lines are measured. The lines form at different atmospheric heights. These Doppler shifts allow to infer the time-dependent velocities $v(t)$ at the formation heights of these lines. Fleck & Deubner observed a low lying Fe I line formed at 200 km and one of the Ca II IRT (infrared triplet) lines, which on basis of semi-empirical chromosphere models originates at 1500 km. After long time-series of velocity fluctuations $v(t)$ in these two lines

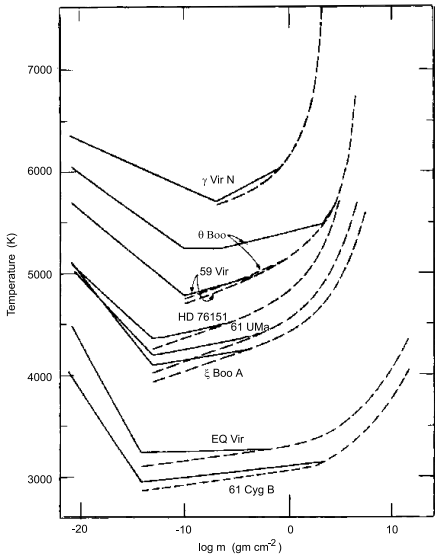

Fig. 29. Semi-empirical stellar chromosphere models based on Ca II K line fits (*solid*), after Kelch, Linsky & Worden (1979). Radiative equilibrium photosphere models are shown *dashed*

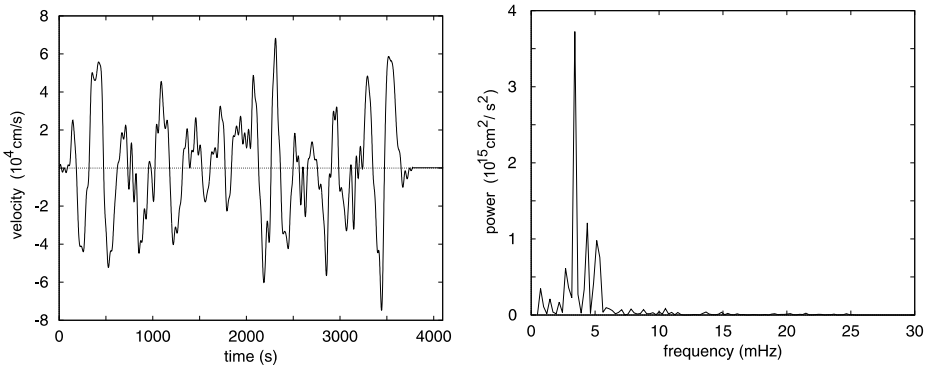

Fig. 30. Left: Velocity. Right: power spectrum in an Fe I line observed by Lites, Rutten & Kalkofen (1993, see Theurer, Ulmschneider & Kalkofen 1997) at a height of $z = 250$ km

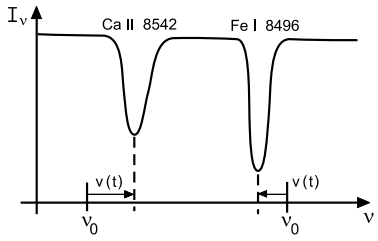

Fig. 31. Simultaneous Doppler measurements of velocity fluctuations in a low lying Fe I line and a Ca II IRT line at great height

are recorded, Fourier transforms

$$F(\omega) = |\tilde{v}(\omega)|\, \mathrm{e}^{\mathrm{i}\varphi(\omega)} = \int_{-\infty}^{+\infty} v(t)\mathrm{e}^{-\mathrm{i}\omega t}\mathrm{d}t \;, \tag{13}$$

can be computed for each line and a cross-correlation can be formed

$$CC(\omega) = |\tilde{v}_{\mathrm{Ca}}(\omega)\tilde{v}^*_{\mathrm{Fe}}(\omega)|\, \mathrm{e}^{\mathrm{i}\Delta\varphi(\omega)} \;, \tag{14}$$

where $\Delta\varphi(\omega) = \varphi_{\mathrm{Ca}}(\omega) - \varphi_{\mathrm{Fe}}(\omega)$ is the phase difference between acoustic velocity fluctuations detected at the two different heights. The frequency dependence of this phase difference provides information about the nature of the acoustic waves. Figure 32 shows the different phase behaviour of propagating and standing acoustic waves. On the left panel for a certain frequency, the wavelength λ of the acoustic wave just fits into the distance interval Δz between the heights where the cores of the Ca and Fe lines are formed. Here one has a phase difference of 0°. If the acoustic frequency is increased and $3/2\lambda$ fit into Δz then a

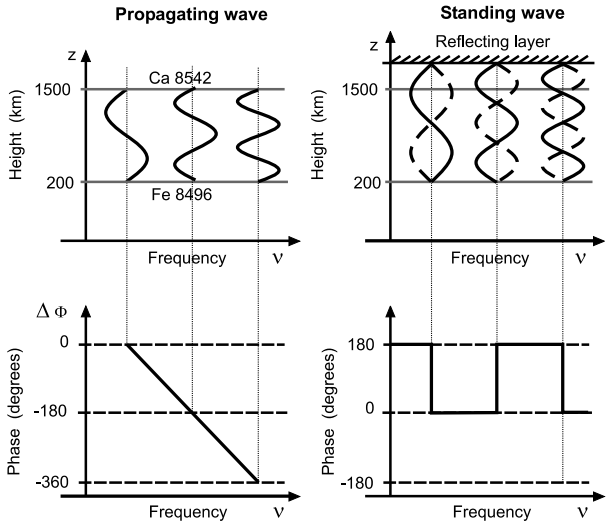

Fig. 32. Phase differences between velocity fluctuations in different spectral lines, for propagating and standing acoustic waves

phase difference of $-180°$ is found, and if 2λ fits, the phase difference is $-360°$ etc.. One sees that for propagating waves one has the relation

$$\Delta\varphi = -360° \left(\frac{\Delta z}{\lambda} - 1 \right) = -360° \left(\frac{\Delta z \ \nu}{c_{\rm phase}} - 1 \right) \ , \qquad (15)$$

where $c_{\rm phase}$ is the phase speed for which the sound speed can be taken. That is, for propagating waves one has a linear dependence of the phase difference on frequency ν. The right panel shows the behaviour of standing waves. As standing waves have infinite phase speed, the phase differences can be either zero or $-180°$ and as function of frequency must undergo sudden phase jumps between these two values.

Figure 33 shows the observed phase differences between the Fe and Ca lines and theoretically computed phase differences on basis of the known sound speed and heights of formation of the two lines. The linear decrease of the phase difference with frequency indicates that acoustic waves of frequency $\nu = \omega/2\pi >$ 5 mHz or wave periods less than 200 s propagate. However, comparison between the two panels shows that theory and observation fit perfectly only if the theoretical height interval $\Delta z = 1300$ km is reduced to 750 km. The big surprise came when in Fig. 34 the Ca II 8542 Å and Ca II 8498 Å IRT lines were compared. The latter line was thought to originate at 1200 km, and thus should have a height interval of $\Delta z = 300$ km relative to the former line. For this height interval the observed phase differences were much too small. This, Fleck & Deubner attributed to a large phase speed (taking $c_{\rm phase} = \infty$ in (15)). They concluded that at 800 km there is a 'magic height' below which acoustic waves are propagating and above which they are standing. This idea causes problems for the acoustic

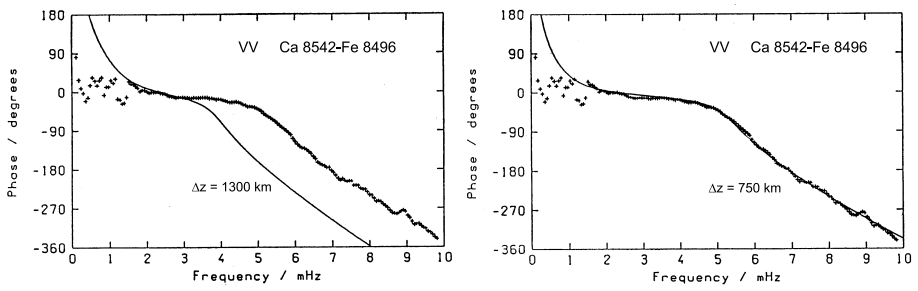

Fig. 33. Observed phase differences between velocity fluctuations in an Fe I line and a Ca II IRT line as function of frequency, after Fleck & Deubner (1989)

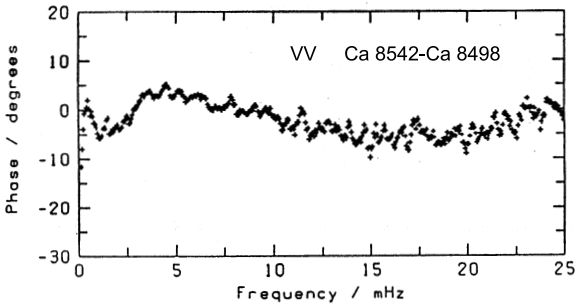

Fig. 34. Observed phase differences between velocity fluctuations in two Ca II IRT lines as function of frequency, after Fleck & Deubner (1989)

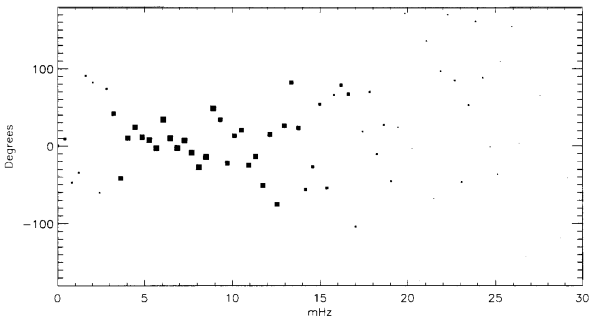

Fig. 35. Theoretical phase differences between velocity fluctuations in two Ca II IRT lines as function of frequency (larger symbols have higher coherence), after Skartlien, Carlsson & Stein (1994)

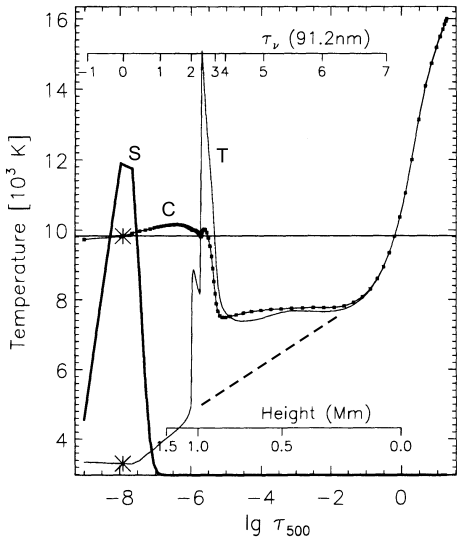

Fig. 36. Snapshot of the temperature (T) and Lyman continuum source function (S) distribution, and the intensity contribution function (C), after Carlsson & Stein (1994)

heating, because standing waves do not heat and thus the energy losses of the middle and high chromosphere could not be balanced.

This picture of standing waves above 800 km was shattered by the Skartlien, Carlsson & Stein (1994) simulations. In their computations they also simulated the Ca II IRT lines and in agreement with the observations found essentially zero phase differences (with some scatter) between these lines as seen in Fig. 35. The reason for this behaviour lies in the nature of the acoustic wave which they discovered in their computation. As seen in Fig. 30, their acoustic input spectrum consists of low frequencies and from these a strong solitary shock formed in their calculation which propagated through the atmosphere and caused the complicated line profile variations in the Ca II H line. After this shock has propagated through the atmosphere, another solitary shock forms etc.. A snapshot of this shock is seen in Fig. 36. It propagates (from the right to the left) on top of the outwardly decreasing (radiative equilibrium) temperature profile (dashed). Behind the shock the temperature rapidly cools down to radiative equilibrium temperatures. To see why this shatters the 'magic height' picture one must realise that the line cores of the Ca II IRT lines form in the post shock region and thus emerge from a thin common height interval Δz behind the shock.

While $\Delta\varphi \approx 0$ in (15) was interpreted by Fleck & Deubner to mean $c_{\rm phase} = \infty$, Stein & Carlsson essentially found that $\Delta\varphi = 0$ comes from $\Delta z = 0$ because both IRT lines are formed at the same height. This very impressive result, which also removed a stumbling block towards a solution of the chromospheric heating problem, gave support to the Carlsson & Stein (1994, 1997) picture and led the authors to draw far reaching conclusions. They claimed that on basis of

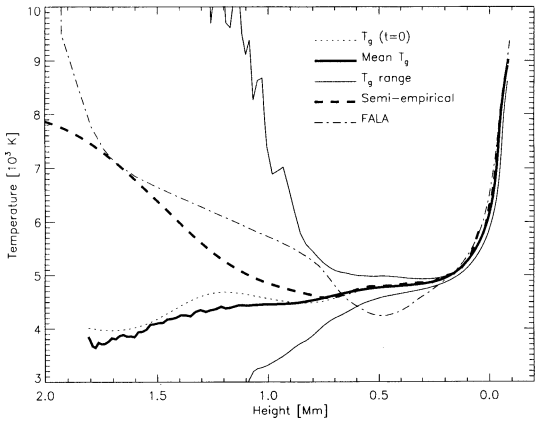

Fig. 37. Time-averaged temperature, after Carlsson & Stein (1994)

their calculations, *classical chromospheres do not exist* and that chromospheres are extremely time-dependent phenomena, in which solitary shocks ever once in a while propagate on top of an outwardly decreasing radiative equilibrium temperature distribution (Carlsson & Stein 1994). Time-averages of their wave calculations resulted in an outwardly decreasing temperature profile (see Fig. 37). This new extremely time-dependent picture shatters the semi-empirical solar and stellar models.

The present author and others (Theurer, Ulmschneider & Kalkofen 1997; Kalkofen, Ulmschneider & Avrett 1999) think that this new view of stellar chromospheres raises a number of unanswered questions and that the old picture of classical chromospheres with an outwardly rising mean temperature although clearly in need of modification should not be discarded prematurely, particularly at great heights in the chromosphere where the kinetic temperature rises to transition layer and coronal values.

One problem with the calculation of Carlsson & Stein most likely is that they took an inadequate acoustic spectrum and therefore used only about 1/10 of the available acoustic energy. To see why taking observed velocity fluctuations leads to a severe underestimation of the available acoustic energy consider the relation between the acoustic wavelength λ and the width Δz of the line contribution function, that is, the height interval over which a spectral line forms. This *contribution function* even for weak lines is not much smaller than about two scale heights $\Delta z = 2H$. In Fig. 38 acoustic waves of different frequency are seen to propagate through the line forming region. The case of $\lambda \gg \Delta z$ results in a full Doppler signal, while for $\lambda \ll \Delta z$ only line broadening is generated (Fig. 38). The critical wavelength where Doppler shifts can no longer be observed occurs when the width of the line contribution function becomes equal to the wavelength of the acoustic wave, that is, when $\lambda = \Delta z = 2H$, and for the Fe I line this is at a wave period of about $P = 50$ s. Buchsbaum (1987) a student of Deubner has

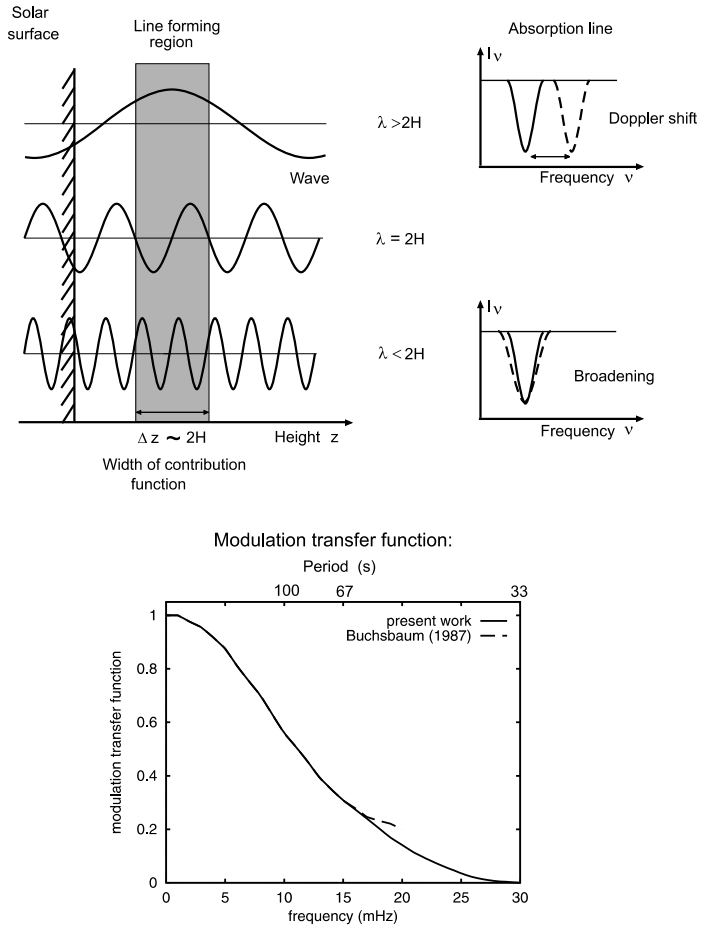

Fig. 38. Influence of the line contribution function on the observability of acoustic waves, and the modulation transfer function (see Theurer, Ulmschneider & Kalkofen 1997)

evaluated a modulation transfer function (see Fig. 38 lower panel) which tells which fraction of a physically present acoustic wave velocity fluctuation can be observed as Doppler shift fluctuation.

To determine the amount of acoustic wave flux actually present at the height of the FeI line, Fig. 39 shows a computation by Theurer, Ulmschneider & Kalkofen (1997) where the acoustic energy spectrum generated in the convection zone at −160 km height is propagated to the height level of the FeI line at about +250 km. The acoustic spectrum present at 250 km (Fig. 39b) is then folded with the modulation transfer function to show what a terrestrial observer will measure as Doppler shift (Fig. 39c). It is seen that only the low frequency component is actually observed (Kalkofen, Ulmschneider & Avrett 1999) which

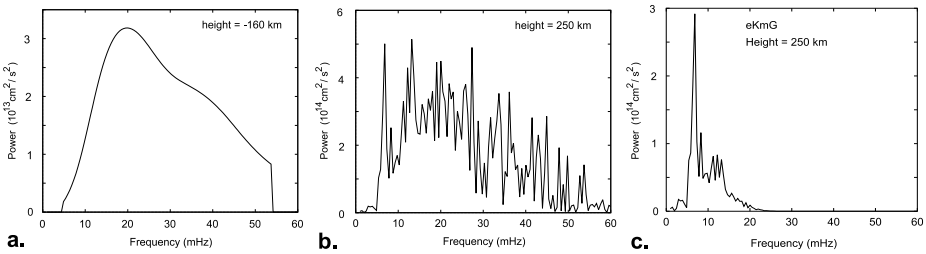

Fig. 39. (**a.**) Acoustic wave spectrum computed in the convection zone at height -160 km. (**b.**) the spectrum after propagation of the wave at height 250 km. (**c.**) spectrum of case **b.** after applying the modulation transfer function. It shows what actually can be observed from this acoustic spectrum as Doppler shifts in a spectral line at 250 km height

contains about 5 to 10% of the actually present acoustic energy. Most of the energy is in high frequencies and cannot be detected (compare Figs. 39b, 39c with Fig. 30). As the low frequency component of the acoustic spectrum is present both in the observations and in the theory, it is clear that the findings of Carlsson & Stein about the solitary shock and the explanation of the Ca II H line core and Ca II IRT phase behaviour will remain unchanged. However, the large amount of acoustic energy in the high frequency component invariably changes the chromospheric heating picture.

9 Realistic Chromospheres

The above discussions show that for realistic chromospheres one must include strongly time-dependent acoustic wave effects, employ a powerful hydrodynamic wave code and use the full acoustic spectrum as input. Figure 40 shows a time sequence of a full acoustic spectrum calculation by Theurer (1998) which, however, did not yet include the full time-dependent treatment of the hydrogen ionisation. It is seen that similarly to Carlsson & Stein strong solitary shocks form and propagate through the atmosphere. But there are also numerous smaller shocks which contribute to the heating of the chromosphere. In Theurer's calculation the strong shock, because of its much greater speed, cannibalises many smaller shocks which enhances the solitary shock picture.

Despite the general agreement with each other of the theoretical simulations of chromospheres by Carlsson & Stein (1994, 1997), Theurer (1998) and Rammacher & Ulmschneider (2003), these computations are not yet fully realistic. Probably a severe shortcoming of all present calculations is that they are one-dimensional (1D) computations. As pointed out by Kalkofen (2003), acoustic waves propagate spherically and the computations should therefore be carried out in a funnel-type geometry. That the acoustic energy generation is nonuniformly distributed over the solar surface has recently been shown by Wunnenberg, Kneer & Hirzberger (2002) but was already suggested long ago by Kuperus

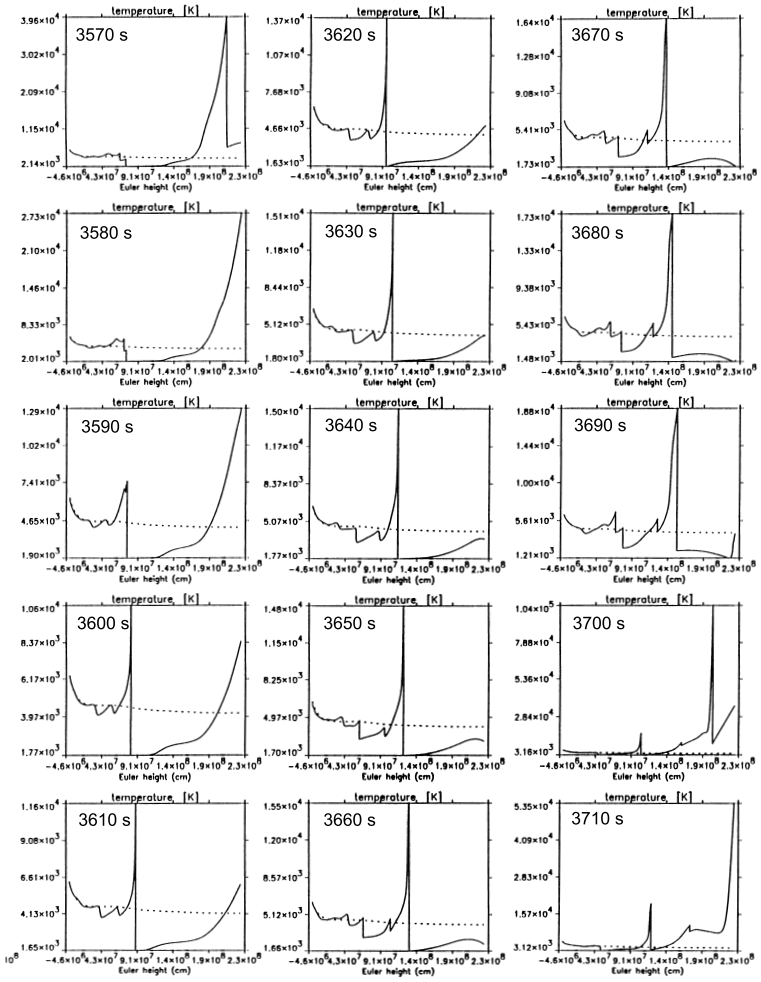

Fig. 40. Series of temperature profiles of a time-dependent acoustic wave computation using an acoustic spectrum in the solar atmosphere, after Theurer (1998)

(1972). The realistic situation is that one has a large number of acoustic sources at discrete locations distributed all over the solar surface from which spherically propagating acoustic waves emanate.

One-dimensional wave computations can only very poorly model this situation. The difficulty is not to simulate the funnel-type geometry in which the wave energy spreads over a progressively larger cross-section, but to take into account the fact that for each energy loss due to a wider tube cross-section there must be an energy gain from neighbouring funnels which cannot be modelled in the 1D calculation. There is another unrealistic property of 1D acoustic wave compu-

tations. In the calculations of Theurer (1998) and Rammacher & Ulmschneider (2003) the strong solitary shock gets much of its power from cannibalising many weaker shocks. That the merging of shocks results in a single stronger shock is a special property of 1D calculations. In a three-dimensional (3D) situation, shocks from waves propagating in different funnels can overlap only at an oblique angle: they amplify only at certain points or lines and thus do not form single merged shocks.

Yet, 3D simulations with many discrete acoustic sources using adequate physics (radiation and ionisation treatments) are presently beyond our computational power. As in a realistic situation the shocks typically are less strong (due to the funnel-type area growth) and stay unmerged (due to intersection at an oblique angle) it appears that presently 1D monochromatic wave calculations are probably the best choice to simulate the general chromospheric heating. This does not contradict the fact that there occasionally are strong shocks.

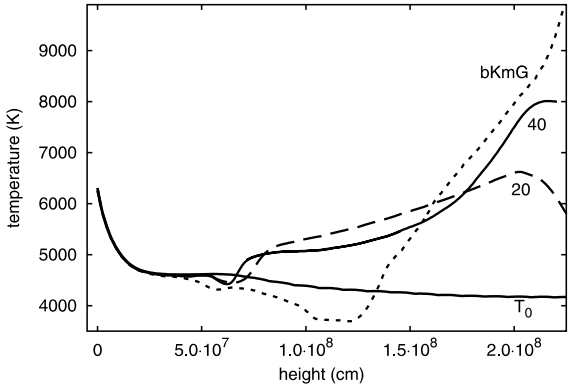

Fig. 41. Averaged solar temperature profile of acoustic wave computations, after Theurer (1998). Monochromatic calculations have periods $P = 20$ and 40 s, bKmG displays a computation with an acoustic spectrum

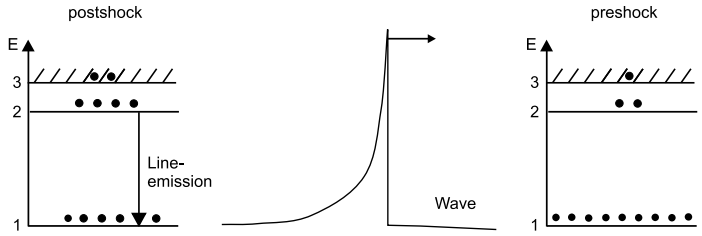

Fig. 42. Change of energy level populations before and after transit of a strong shock

Figure 41 shows a comparison of the mean chromospheric temperatures from two acoustic wave calculations using monochromatic waves and one with a full acoustic spectrum. The mean temperatures are produced by time-averaging temperature distributions like in Figs. 23 and 40. It is seen that the monochromatic wave calculations generate classical chromospheres. Yet the acoustic spectrum calculation at greater height also shows a classical chromospheric temperature rise (see also Theurer, Ulmschneider & Cuntz 1997).

To discuss the treatments of the hydrogen ionisation consider in Fig. 42 the population of energy levels of important chromospheric atoms before and after a strong shock travels through a gas element. For simplicity we take a hydrogen atom with two bound levels 1 and 2 and a continuum level 3. In the cold phase, before the shock arrives, the populations n_1, n_2, n_3 are concentrated to the ground state, while after the shock has passed the high temperature in the post-shock phase is supposed to lead to an increased population of the higher atomic levels. This increased population by transitions to the ground state should produce enhanced radiation losses from the atmosphere. This behaviour is indeed found when the populations are calculated (called NLTE treatment) using the individual radiative R_{ij} and collisional C_{ij} processes and solving *statistical rate equations* like e.g., the following for the ground level 1 of the three level atom:

$$n_2(R_{21} + C_{21}) + n_3(R_{31} + C_{31}) - n_1(R_{12} + C_{12} + R_{13} + C_{13}) = 0 \,. \qquad (16)$$

Here the two left hand terms are the gains of electrons from the upper levels 2 and 3 and the third term is the loss of electrons from level 1. In most of our work we solve this equation consistently with the instantaneous temperature. In reality, however, the increase of the population of the high levels, particularly the continuum level 3, takes a finite time. Here it must be realised that the bound-bound transitions are very rapid while the bound-continuum transitions are slower by many orders of magnitude. That means it is not good enough to solve the statistical rate equations, one must actually solve the *time-dependent rate equation*

$$\frac{\mathrm{d}n_1}{\mathrm{d}t} = n_2(R_{21} + C_{21}) + n_3(R_{31} + C_{31}) - n_1(R_{12} + C_{12} + R_{13} + C_{13}) \,. \qquad (17)$$

The time-dependence delays the buildup of the population of the high levels. This delay can be so severe that the level populations essentially decouple from the spiky temperature variation in the wave. Therefore the consequence of solving the statistical rate equations instead of the time-dependent rate equations is that one greatly overestimates the radiation losses in strong shock computations (this error is less severe for weak shocks which occur in a monochromatic wave computation). In wave calculations which treat the hydrogen ionisation with a time-dependent rate equation the large relaxation time of the continuum transitions ($t_{\mathrm{Rel}} \approx 1/R_{31}$) leads to a degree of ionisation in the middle and high chromosphere which practically is decoupled from the temperature fluctuations. Figure 43 shows snapshots of acoustic wave calculations of this type. In the monochromatic wave calculation on the left panel it is seen that the degree of

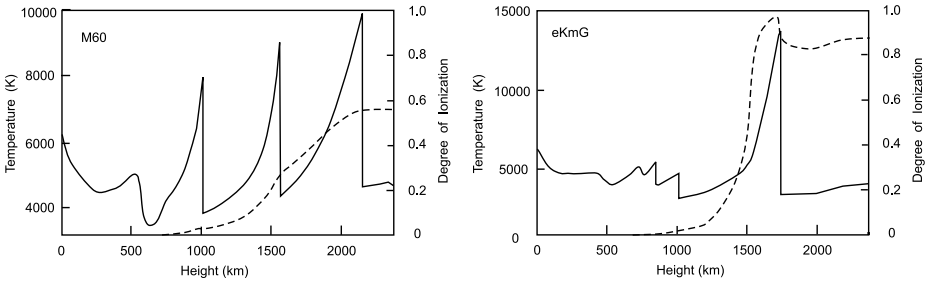

Fig. 43. Temperature (*solid*) and degree of ionisation (*dashed*) in acoustic wave calculations with time-dependent hydrogen ionisation and a flux $F_A = 1 \times 10^8$ erg cm^{-2} s^{-1}. Left: Monochromatic acoustic wave with period $P = 60$ s (M60). Right: acoustic wave with an eKmG spectrum, after Rammacher & Ulmschneider (2003)

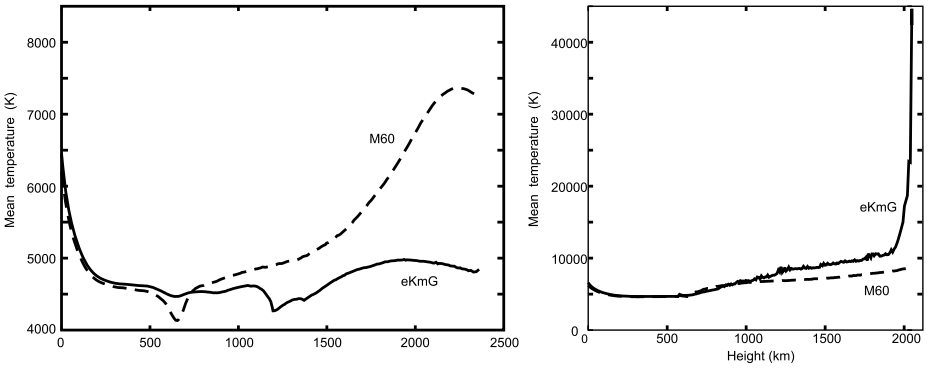

Fig. 44. Different mean temperature evaluations in the wave calculations of Fig. 43. Left: temporal averaging. Right: Ionisation temperature from the Saha equation using averaged number densities n_1, n_3, n_e, after Rammacher & Ulmschneider (2003)

ionisation is practically unaffected by the temperature fluctuations at the shocks. Only if a shock is very strong as in the wave calculation with an acoustic spectrum (right panel) does the degree of ionisation in the post-shock region react to the temperature jump in the way expected from Fig. 42.

Surprisingly, time-averaging the fluctuating temperature in the gas elements (Fig. 44, left panel) gives a classical chromosphere (like in Figs. 41, 23) only for the monochromatic wave, while for the acoustic spectrum calculation essentially no temperature rise is found. This situation is very different when the ionisation temperature is considered (Fig. 44 right panel). The ionisation temperature T_i is the temperature which satisfies the NLTE Saha-equation

$$\frac{n_1}{n_3} = n_e \left(\frac{h^2}{2\pi m_e k T_\mathrm{i}} \right)^{3/2} \mathrm{e}^{\frac{E_H}{kT_\mathrm{i}}} \,, \tag{18}$$

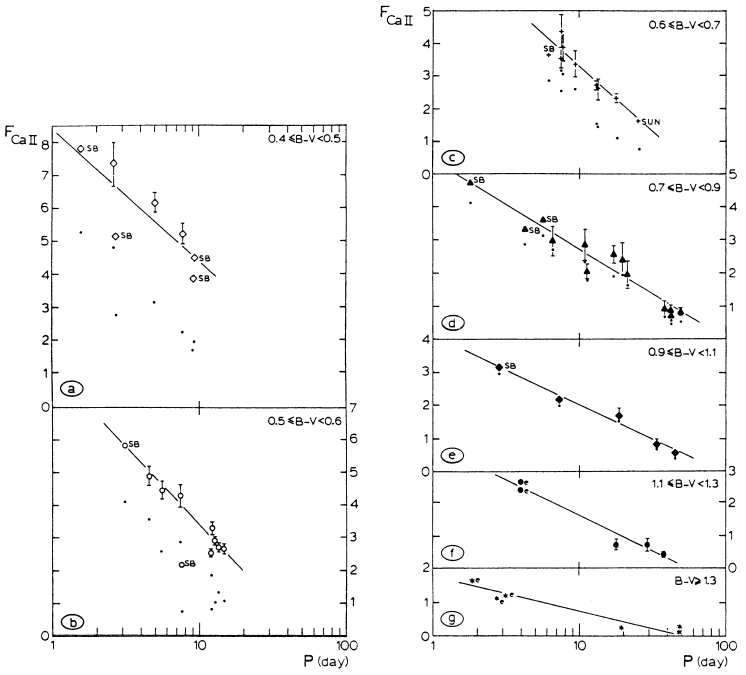

Fig. 45. Rotation–chromospheric Ca II emission correlations, after Rutten (1986). The panels a to g are for stars in different B − V ranges of width 0.1 from B − V = 0.4 to greater than 1.3

when the time-averaged number densities n_1, n_3 and n_e are used. Here h is the Planck constant, m_e the electron mass, k the Boltzmann constant and $E_{\rm H}$ the ionisation energy of hydrogen. The ionisation temperature shows a classical temperature rise in the chromosphere together with the rapid rise in the transition layer. That the acoustic spectrum calculation shows a more pronounced temperature rise is explained from the fact that this wave leads to a higher degree of ionisation (compare the two cases in Fig. 43).

10 Magnetic Chromospheres

We now consider magnetic chromospheres. As discussed above, the great problem to understand magnetic chromospheres is that many heating mechanisms exist. A basic task therefore is to identify which of these are the relevant ones. This is difficult as only for a few magnetic mechanisms is it presently known how much mechanical energy is available. While the situation is relatively good for magnetic body waves (although calculations of the energy generation of torsional Alfvén waves are still missing) a computation of the amount of energy available for e.g., micro flare heating is lacking, as is an evaluation of the energy generation of surface waves.

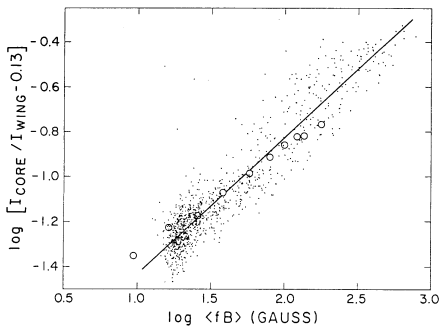

Fig. 46. Magnetic flux–chromospheric Ca II emission correlation for the Sun, after Schrijver et al. (1989)

Two important observational effects can be used to identify the magnetic heating mechanisms: the so called *rotation–chromospheric emission correlation* and *magnetic flux–chromospheric emission correlation*. Figure 45 shows that in a given range of colour B − V (or $T_{\rm eff}$) the chromospheric Ca II emission is strongly correlated with the stellar rotation period. Rapidly rotating stars have large chromospheric emission while the emission of the stars with longest rotation period decreases to the basal flux emission level. The other correlation is seen in Fig. 46 where the observed excess (relative to the basal flux) Ca II emission intensity is plotted against the measured magnetic flux. These observations indicate that higher magnetic flux results in greater chromospheric emission. Combining the two correlations one finds that the more rapidly a star rotates the more magnetic flux it has on its surface.

As discussed above it is found that on the Sun the magnetic field appears in sunspots and plage regions but also in a large number of thin isolated magnetic flux tubes. These tubes are distributed more or less uniformly over the entire solar surface and show a concentration towards the boundaries of supergranulation cells. In the Ca II K and He II 304 Å lines as well as other chromospheric and transition layer lines the supergranulation boundaries show intense emission associated with the magnetic field, called *chromospheric network*.

Carrying most of the stellar magnetic flux $\Phi_{\rm M} = |B| A_{\rm M}$ these magnetic flux tubes have a magnetic filling factor $f = A_{\rm M}/A_*$, defined as the ratio of the area covered by magnetic fields $A_{\rm M}$ to the total area A_* at the stellar surface. The Sun has a small filling factor $f \approx 0.02$ (see Fig. 47) while rapidly rotating stars can have $f > 0.4$. The diameter of these flux tubes grows, until in the middle chromosphere (for the Sun at around 1500 km height) the magnetic fields fill out the entire available space (Fig. 47). It was also mentioned above that perturbed by external turbulence at the top of the convection zone, longitudinal, transverse and torsional MHD waves are generated in these tubes.

Note that presently there is no way to specify the magnetic flux $\Phi_{\rm M}$ for stars from first principles on basis of the four parameters $T_{\rm eff}$, g, $Z_{\rm m}$ and $P_{\rm Rot}$. This

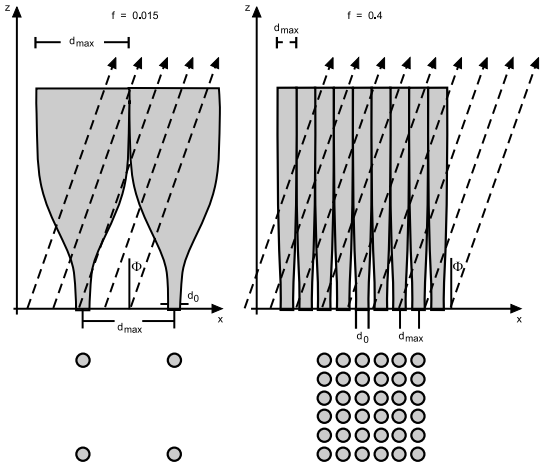

Fig. 47. Flux tube models of different filling factors f, for the solar case (left panels) and the case $f = 0.4$ (right panels). The lower panels show the cross-sections at the stellar surface

awaits the successful development of a dynamo theory. However, it is possible to progress by constructing magnetic chromosphere models of stars by assuming different magnetic filling factors f. These models can be characterised by four parameters $T_{\rm eff}$, g, $Z_{\rm m}$ and f. We suppose that similar to the Sun the magnetic field on other stars is also dominated by a large number of thin isolated magnetic flux tubes and that the field strength of these tubes at the stellar surface is $B = 0.85 B_{\rm eq} = 0.85\sqrt{8\pi p}$ where p is the external gas pressure. In addition we assume that the diameter of the flux tubes at the stellar surface is about a scale height. Figure 47 shows flux tube models for stars of the same $T_{\rm eff}$ and g but different filling factors f computed with these assumptions.

Using such tube models, magnetic wave energy fluxes and wave spectra can be calculated for longitudinal and transverse MHD waves. For longitudinal wave fluxes using an analytical approach see Musielak, Rosner & Ulmschneider (1989, 2000, 2002), Musielak et al. (1995), and with a numerical approach Ulmschneider & Musielak (1998), Ulmschneider, Musielak & Fawzy (2001). For transverse wave fluxes using an analytical approach see Musielak & Ulmschneider (2001, 2002a, 2002b), and for the numerical approach see Huang, Musielak & Ulmschneider (1995) with a correction discussed in Ulmschneider & Musielak (1998). Figure 48 displays and compares some of these fluxes. It is found that roughly transverse waves are by a factor of 30 more efficiently generated than longitudinal waves.

On basis of these fluxes and spectra one calculates the propagation of longitudinal MHD waves along the flux tubes together with the shock heating. Here the thin flux tube approximation was used. In addition, employing acoustic wave computations, the heating of the medium outside the tubes is computed. Same as for the acoustic wave calculations discussed above, monochromatic magnetic waves were employed with periods taken from the maximum of the longitudinal

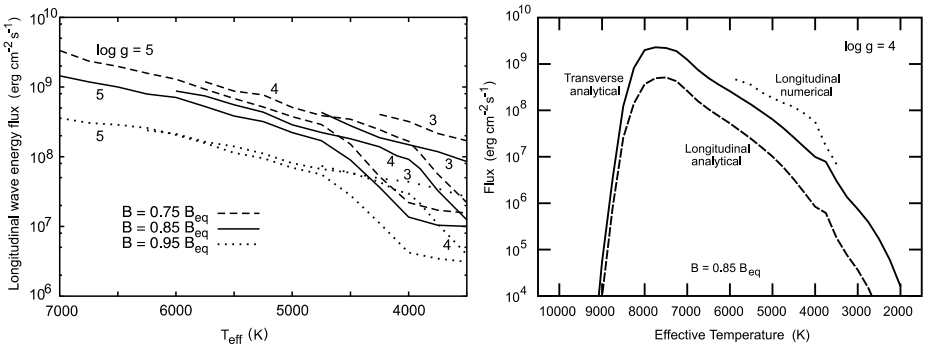

Fig. 48. Longitudinal tube wave fluxes (numerical), after Ulmschneider, Musielak & Fawzy (2001) (left), longitudinal and transverse tube wave fluxes, after Musielak & Ulmschneider (2002a) (right)

wave energy spectrum. Similarly as for our pure acoustic wave computations, using a multi-ray transfer code, the Mg II and Ca II line profiles emerging from the forest of magnetic flux tubes are then evaluated using ray-paths as shown in Fig. 47, and finally the emission core fluxes were compared with observations.

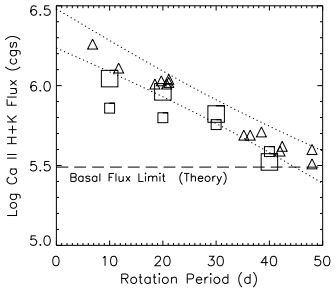

Fig. 49. Rotation–Ca II core emission flux relation of a sample of K2V stars (triangles) compared to that of simulated core emissions on basis of MHD wave heating (squares), after Cuntz et al. (1999). The *dotted* lines indicate the observed emission–rotation correlation similar as in Fig. 45, the *dashed* line gives the theoretical basal flux which the stars would have if they did not rotate

The result of such a comparison for stars of spectral type K2V are shown in Fig. 49. Here magnetic field strengths and rotation periods have been measured and the generation, propagation and heating of longitudinal waves was calculated. Large squares assume a uniform distribution of the magnetic tubes over the stellar surface while small squares are for distributions with a pronounced network structure. It is seen that for the K2V stars, the observed rotation–

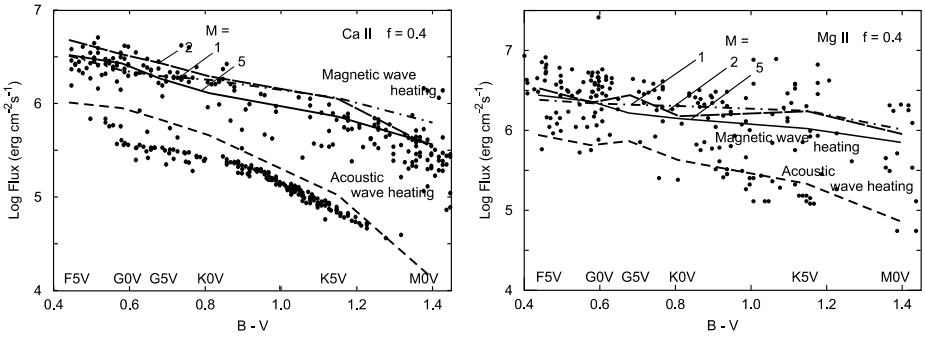

Fig. 50. Empirical core emission fluxes of Ca II (dots, left) and Mg II lines (dots, right), compared with theoretical fluxes for pure acoustic wave heating and for magnetic wave heating in flux tubes with an area filling factor of $f = 0.4$, after Fawzy et al. (2002b)

chromospheric emission correlation is relatively well reproduced by the theoretical simulations.

Figure 50 shows a more extensive comparison of theoretical emission fluxes with observations for late-type stars by Ulmschneider et al. (2001) and Fawzy et al. (2002a, b). Shown dashed are theoretical models with pure acoustic wave heating for stars with no magnetic fields ($f = 0$). They agree fairly well with the observed emission of basal flux stars. The discrepancy for F5V to G5V stars for the Ca II emission is attributed to the large errors in subtracting the photospheric background emission in the observations and to inaccuracies of the theoretical computations (see Fawzy et al. 2002a, b).

Theoretical MHD wave heating models are indicated solid. To show the maximum that MHD wave heating can generate, a maximum magnetic filling factor of $f = 0.4$ was assumed. The reason for this is that with $f = 0.4$ the main energy carrying convective bubbles (with diameters of a scale height) still fit in the space outside the flux tubes to permit efficient MHD-wave generation (see Fig. 47). To allow for additional wave energy by mode-coupling from transverse waves the longitudinal wave flux in some cases were multiplied by factors $M = 1$ to $M = 5$ (see Fig. 50). A maximum factor $M = 5$ due to mode-coupling was assumed to be realistic, particularly in view of the fact that transverse waves are much more efficiently produced as mentioned above. As the amount of longitudinal wave energy generation due to mode-coupling cannot yet be reliably computed the calculations with different values of M show the theoretical uncertainty at present.

When comparing the theoretical emission fluxes for the magnetic cases with the observed Ca II and Mg II saturation limits it has to be noted (like in the acoustic case) that they are obtained from fully ab initio calculations which only specify the four parameters $T_{\rm eff}$, g, $Z_{\rm m}$ and f. Thus the theoretical steps to construct the convection zone and magnetic flux tube models, the wave generation process, the wave propagation and 2D radiative transfer in the spectral lines are

expected to lead to considerable cumulative errors. It is therefore interesting that the magnitude of the emission and its $T_{\rm eff}$-dependence as well as the emission variation with the filling factor appears to be in relatively good agreement with the observations. Such an agreement would not be expected if the wave heating mechanism were wrong or only a minor contribution to the total chromospheric heating. We conclude therefore that the agreement confirms that longitudinal tube waves are the main heating mechanism of magnetic chromospheres.

Figure 50 also shows that while the variation of the filling factor covers the entire chromospheric emission variability (between the basal flux line and the saturation limit) for Ca II, there appears to be a gap between the theoretical simulations and the observed maximum of the Mg II emissions. Because the Ca II emission is generated at lower chromospheric heights than the Mg II emission we feel that this gap indicates that in the highest chromosphere another non-wave magnetic heating mechanism comes into play. It is possible that this missing magnetic heating mechanism consists of microflare reconnective heating proposed by Parker (see Sect. 4.10). This verdict, however, must await the study of the torsional waves and of the role of surface waves.

11 Conclusions

Chromospheres and coronae are hot outer layers of late-type stars which are dominated by mechanical heating. Similarly as for the stellar interior and the stellar atmosphere (photosphere) the average behaviour of these layers and the magnitude of their variability should be describable by only 4 basic parameters, effective temperature $T_{\rm eff}$, gravity g, metallicity $Z_{\rm m}$ and surface rotation period $P_{\rm Rot}$. The connection of the chromospheric and coronal structures with these 4 parameters has so far not been completely unravelled but significant progress has been made.

1. There are two classes of heating mechanisms (see Table 1): hydrodynamic and magnetic mechanisms. The latter are further subdivided in AC-mechanisms (waves) and DC-mechanisms (current sheets). All suggested heating mechanisms are thought to work for stars, given the right situation and magnetic field geometry, because they are known to work in terrestrial applications. However, it is important to identify the main processes for the individual stellar layers and magnetic regions.

2. The turbulent flow fields of the surface convection zones of late-type stars generate acoustic waves. Propagating to the outer layers these waves form shocks which heat the chromospheres. Acoustically heated chromospheres depend only on three basic parameters $T_{\rm eff}$, g, $Z_{\rm m}$, as convection zones do not vary with rotation.

3. From the computed acoustic energy fluxes, theoretical shock heated chromospheres can be constructed and the Ca II and Mg II line core emission simulated. These simulations reproduce the observed basal flux line, that is, the lower limit of chromospheric emission for main sequence stars, giants and low

metallicity stars. This shows that acoustic waves are very likely the main heating mechanism for the low chromospheres of late-type stars.

4. When propagating from the convection zone, the low frequency part of the acoustic wave spectrum generates strong solitary shocks, which explain the observed solar Ca II H line profile variations and phase relations between the Ca II IRT lines. The propagating wave spectrum also generates numerous weaker shocks which together with the strong shocks produce a classical chromosphere, that is, a layer with an outwardly rising mean temperature distribution, most easily seen in the degree of ionisation and the ionisation temperature.

5. In the high chromosphere the dominant cooling mechanism (H I Lyα, Ca II H+K+IRT and Mg II h + k lines) get destroyed by the ionisation of H, Ca II and Mg II. This causes the heating to become unbalanced, which generates the transition layer temperature rise to the corona.

6. Rotation (described by the fourth basic parameter $P_{\rm Rot}$) together with convection produces the magnetic fields of late-type stars. Since the dynamo theory is so far not sufficiently developed to predict the stellar magnetic flux from the 4 basic parameters, observations must be used to unravel the magnetic heating mechanisms. These observations are mainly the rotation–chromospheric emission and magnetic flux–chromospheric emission correlations, the magnitude and $T_{\rm eff}$-dependence of the basal and saturation limits of chromospheric emission, and magnetic field strength measurements, although the latter tend to measure sunspot and plage fields and not the large numbers of small scale flux tubes where most of the magnetic flux is.

7. For various flux tube models and filling factors f of magnetic flux covering the star, longitudinal and transverse MHD wave energy fluxes can be computed and the wave propagation along these magnetic flux tubes as well as in the non-magnetic regions performed. This generates two-component stellar chromosphere models and allows to simulate the chromospheric emission. For K2V stars, where magnetic field observations are available, the observed rotation–emission relation could be reproduced.

8. For simulations using a maximum filling factor of $f = 0.4$ and a maximum amount of longitudinal and transverse MHD wave energy it was found that for Ca II the observed saturation limit of chromospheric emission could be reproduced, but that the limit for Mg II could not be reached. This indicates that the magnetic regions of the middle and upper chromosphere are heated by MHD wave dissipation, but that at the top of the chromosphere another non-wave heating mechanism, possibly reconnective microflare heating operates. This conclusion is tentative as the role of the heating by torsional Alfvén waves and surface waves must be studied.

9. To clarify the zoo of coronal heating processes much further work remains to be done.

Acknowledgements

The author thanks the Deutsche Forschungsgemeinschaft for generous provision of funds for projects Ul57/28-1, Ul57/30-1 and Ul57/32-1.

References

1. Brueckner, G. E., 1981, in Solar Active Regions, Skylab Solar Workshop III, ed. F. Q. Orrall, (Colorado Assoc. Univ. Press) 113
2. Brueckner, G. E., & Bartoe, J.-D. F., 1983, ApJ, 272, 329
3. Buchholz B., & Ulmschneider P., 1994, in Cool Stars, Stellar Systems and the Sun, ed. J. P. Caillault, ASP Conf. Series 64, 363
4. Buchholz, B., Ulmschneider, P., & Cuntz M., 1998, ApJ, 494, 700
5. Buchsbaum, G., 1987, Diplom thesis, Univ. Würzburg, Germany
6. Carlsson, M., & Stein, R. F., 1994, in Chromospheric Dynamics, Proc. Mini-Workshop, ed. M. Carlsson, Inst. Theor. Astroph., Oslo, p. 47
7. Carlsson, M., & Stein, R. F., 1995, ApJ, 440, L29
8. Carlsson, M., & Stein, R. F., 1997, ApJ, 481, 500
9. Chen, F. F., 1974, Introduction to Plasma Physics (Plenum Press, New York)
10. Cuntz, M., Rammacher, W., & Ulmschneider, P., 1994, ApJ, 432, 690
11. Cuntz, M., Rammacher, W., & Ulmschneider, P., Musielak, Z. E., Saar, S. H., 1999, ApJ, 522, 1053
12. Fawzy, D., Rammacher, W., Ulmschneider, P., Musielak, Z. E. & Stępień, K., 2002a, ApJ, 386, 971
13. Fawzy, D., Ulmschneider, P., Stępień, K., Musielak, Z. E., & Rammacher, W. 2002b, ApJ, 386, 983
14. Fleck, B., & Deubner, F.-L., 1989, A&A, 224, 245
15. Goldstein, M. E., 1976, Aeroacoustics (McGraw-Hill, New York) p. 94
16. Heyvaerts, J., & Priest, E. R., 1983, A&A 117, 220
17. Hollweg, J. V., 1983, in Solar Wind, ed. V, M. Neugebauer, NASA CP-2280, 5
18. Hollweg, J. V., Jackson, S., & Galloway, D., 1982, Sol. Phys., 75, 35
19. Huang, P., Musielak, Z. E., & Ulmschneider, P., 1995, A&A, 297, 579
20. Kalkofen, W., 2003, in Current Theoretical Models and High Resolution Solar Observations: Preparing for ATST, eds. A. A. Pevtsov & H. Uitenbroek, ASP Conference Series Vol. 286, 385
21. Kalkofen, W., Ulmschneider, P., & Avrett, E. H., 1999, ApJ, 521, L141
22. Kelch, W. L., Linsky, J. L., & Worden, S. P., 1979, ApJ, 229, 700
23. Kippenhahn, R., & Weigert, A., 1990, Stellar Structure and Evolution (Springer, Berlin)
24. Kuperus, M., 1972, Sol. Phys., 22, 257
25. Lites, B. W., Rutten, R. J., & Kalkofen, W., 1993, ApJ, 414, 345
26. Mitra-Kraev, U., & Benz, A. O., 2001, A&A, 373, 318
27. Muller, R., Roudier, Th., Vigneau, J., & Auffret, H., 1994, A&A, 283, 232
28. Musielak, Z. E., & Ulmschneider, P., 2001, A&A, 370, 541
29. Musielak, Z. E., & Ulmschneider, P., 2002a, A&A, 386, 606
30. Musielak, Z. E., & Ulmschneider, P., 2002b, A&A, 386, 615
31. Musielak, Z. E., Rosner, R., & Ulmschneider, P., 1989, ApJ, 337, 470
32. Musielak, Z. E., Rosner, R., Stein, R. F., & Ulmschneider, P., 1994, ApJ, 423, 474
33. Musielak, Z. E., Rosner, R., Gail, H. P., & Ulmschneider P., 1995, ApJ, 448, 865

34. Musielak, Z. E., Rosner, R., & Ulmschneider, P., 2000, ApJ, 541, 410
35. Musielak, Z. E., Rosner, R., & Ulmschneider, P., 2002, ApJ, 573, 418
36. Narain, U., & Ulmschneider, P., 1990, Space Sci. Rev., 54, 377
37. Narain, U., & Ulmschneider, P., 1996, Space Sci. Rev., 75, 453
38. Parker, E. N., 1981, in Solar phenomena in stars and stellar systems, Proc. Adv. Study Inst. Bonas, eds. R. M. Bonnet, & A. K. Dupree, (D. Reidel, Dordrecht) 33
39. Parker, E. N., 1991 in Mechanisms of Chromospheric and Coronal Heating, eds. P. Ulmschneider, E. R. Priest, & R. Rosner, (Springer, Berlin) 615
40. Priest, E. R., 1991, in Mechanisms of Chromospheric and Coronal Heating, eds. P. Ulmschneider, E. R. Priest, & R. Rosner, (Springer, Berlin) 520
41. Rammacher, W., & Ulmschneider, P., 2003, ApJ, (in press)
42. Rutten, R. G. M., 1986, A&A, 159, 291
43. Rutten, R. G. M., Schrijver, C. J., Lemmens, A. F. P., & Zwaan, C., 1991, A&A, 252, 203
44. Schrijver, C. J., & Zwaan, C., 2000, Solar and Stellar Magnetic Activity, (Cambridge University Press, Cambridge)
45. Schrijver, C. J., Coté, J., Zwaan, C., & Saar, S. H., 1989, ApJ, 337, 964
46. Skartlien, R., Carlsson, M., & Stein, R. F., 1994, in Chromospheric Dynamics, Proc. Mini-Workshop, ed. M. Carlsson, Inst. Theor. Astroph., Oslo, p. 79
47. Solanki, S. K., 1993, Space Sci. Rev., 63, 1
48. Stenflo, J. O., 1994, Solar Magnetic Fields (Kluwer, Dordrecht)
49. Strauss, H. R., 1991, Geophys. Res. Let., 18, 77
50. Theurer, J., 1998, Ph. D. Thesis, Univ. Heidelberg, Germany
51. Theurer, J., Ulmschneider, P., & Cuntz, M., 1997, A&A, 324, 587
52. Theurer, J., Ulmschneider, P., & Kalkofen, W., 1997, A&A, 324, 717
53. Tu, C.-Y., & Marsch, E., 1997, Sol. Phys., 171, 363
54. Tu, C.-Y., & Marsch, E., 2001a, A&A, 368, 1071
55. Tu, C.-Y., & Marsch, E., 2001b, JGR, 106, 8233
56. Ulmschneider, P., 1996 in Cool Stars, Stellar Systems and the Sun, eds. R. Pallavicini, & A. K. Dupree, Astr. Soc. Pacific Conf. Ser. 109, 71
57. Ulmschneider, P., & Musielak, Z. E., 1998, A&A, 338, 311
58. Ulmschneider, P., Theurer, J., & Musielak, Z. E., 1996, A&A, 315, 212
59. Ulmschneider, P., Theurer, J., Musielak, Z. E., & Kurucz, R., 1999, A&A, 347, 243
60. Ulmschneider, P., Musielak, Z. E., & Fawzy, D. E., 2001, A&A, 374, 662
61. Ulmschneider, P., Fawzy, D., Musielak, Z. E., & Stępień, K., 2001, ApJ, 559, L167
62. Vernazza, J. E., Avrett, E. H., & Loeser, R., 1981, ApJS, 45, 635
63. Wood, B. E., Linsky, J. L., & Ayres, T. R., 1997, ApJ, 478, 745
64. Wunnenberg, M., Kneer, F., & Hirzberger, J., 2002, A&A, 395, L51
65. Zhugzhda, Y., Bromm, V., & Ulmschneider, P., 1995, A&A, 300, 302
66. Ziegler, U., & Ulmschneider, P., 1997, A&A, 327, 854